A constitutive model for clays and plastic silts in plane-strain earthquake engineering applications

by

Ross W. Boulanger [a]
(Corresponding author: rwboulanger@ucdavis.edu)

and

Katerina Ziotopoulou [b]
(kziotopoulou@ucdavis.edu)

[a] Professor, Department of Civil and Environmental Engineering,
University of California, Davis, USA

[b] Assistant Professor, Department of Civil and Environmental Engineering,
University of California, Davis, USA

Authors' final manuscript before copyediting (August 2019).
Published in Soil Dynamics and Earthquake Engineering, 127(2019): 105832,
10.1016/j.soildyn.2019.105832.

Abstract

A plasticity model for representing clays and plastic silts, as opposed to purely nonplastic silts or sand, in geotechnical earthquake engineering applications is presented. The PM4Silt model builds on the framework of the stress-ratio controlled, critical state based, bounding surface plasticity PM4Sand model, and is coded as a user defined material for use with the program FLAC. The model was developed to provide reasonable approximations of monotonic undrained shear strength, cyclic undrained shear strength, and shear modulus reduction and hysteretic damping responses. The model does not include a cap, and therefore is not suited for simulating consolidation or reconsolidation settlements (i.e., volumetric strains) or strength evolution with consolidation stress or seismic loading history. The primary input parameters are the undrained shear strength ratio (or undrained shear strength), the shear modulus coefficient, and the contraction rate parameter. All secondary input parameters are assigned default values based on a default calibration, but may be adjusted when calibrating against advanced laboratory test data or performing sensitivity studies. The calibration process is described and illustrated by calibrations for three different normally consolidated, fine-grained soils with plasticity indices ranging from 4 to 20. The model is shown to provide reasonable approximations of behaviors important to many earthquake-engineering applications and to be relatively easy to calibrate.

1. INTRODUCTION

Nonlinear seismic deformation analyses in geotechnical practice require approximating the stress-strain responses of a broad range of soil types including sand-like soils that may liquefy and clay-like soils that may cyclically soften during strong shaking. A number of advanced constitutive models for representing sand-like soils are available in the finite element or finite difference programs most commonly used in engineering practice, whereas the options for representing clay-

like soils in these same programs are relatively limited. Consequently, it is common for clay-like soils to be represented in nonlinear dynamic analyses (NDAs) (e.g., Rampello et al. 2009, Luque and Bray 2017, Hadidi et al. 2017, Tasiopoulou et al. 2018) using relatively simple hysteretic or elastic-plastic constitutive models (e.g., Schanz et al. 1999, Naesgaard 2011, Itasca 2016) that cannot adequately simulate the cyclic softening and degradation responses of soft clays and plastic silts. More advanced constitutive models for simulating cyclic loading responses and cyclic softening of clays have been developed (e.g., Dafalias et al. 2006, Yang et al. 2008, Taiebat et al. 2010, Seidalinov and Taiebat 2014, Hu and Liu 2015, Ni et al. 2015), but there remains a need for implementation and validation of these types of models in the various analysis programs most commonly used in engineering practice. Lastly, intermediate soils such as low-plasticity silts, sandy silts, and sandy clays can be particularly challenging to represent in an NDA if the soil's cyclic loading responses are intermediate to those that are reasonably approximated by constitutive models designed for either sand-like or clay-like behaviors (Bray et al. 2017).

The engineering properties of saturated clays and plastic silts that are of primary concern for many earthquake-engineering applications are: (1) monotonic undrained shear strength, (2) cyclic undrained shear strength and associated stress-strain responses, and (3) secant shear moduli and equivalent damping ratios. Regarding the cyclic undrained shear strength, key features include its dependence on the number of uniform loading cycles, effective overburden stress, and initial static shear stress ratio. For cyclic undrained stress-strain responses, key features include the shape of the hysteretic stress-strain loops (which relates to excess pore pressure generation) and the rate of shear strain accumulation with continued cyclic loading under different initial static shear stress ratios. For secant moduli and damping ratios, the primary focus is on their variation with shear strain amplitude, with the effects of overburden stress sometimes being of secondary interest. The

above monotonic and cyclic loading properties are often of primary concern because they usually have the strongest effects on the dynamic responses and associated deformations obtained in NDAs of various soil and soil-structure systems.

A plasticity model for representing clays and plastic silts (PM4Silt) in geotechnical earthquake engineering applications is presented. The PM4Silt model builds on the framework of the stress-ratio controlled, critical state based, bounding surface plasticity PM4Sand model (Boulanger and Ziotopoulou 2017, Ziotopoulou and Boulanger 2016), and is implemented as a dynamic link library for use with the program FLAC (Itasca 2016). The PM4Silt model includes modifications, relative to PM4Sand, that improve its ability to approximate the monotonic undrained strength, cyclic undrained strength, and secant shear modulus and equivalent damping ratio behaviors of clays and plastic silts (as opposed to those for purely nonplastic silts or sands). The model does not include a cap and therefore is not suited for simulating consolidation processes, predicting consolidation or reconsolidation settlements (i.e., volumetric strains), or predicting the evolution of undrained shear strength with consolidation stress or seismic loading history. The primary input parameters are the undrained shear strength ratio (or undrained shear strength), the shear modulus coefficient, and the contraction rate parameter. All secondary input parameters are assigned default values based on a default calibration, but may be adjusted when calibrating against advanced laboratory test data or performing sensitivity studies. The calibration process is described and illustrated by example responses for three different normally consolidated, fine-grained soils with plasticity indices ranging from 4 to 20. The model is shown to provide reasonable approximations of behaviors important to many earthquake-engineering applications and to be relatively easy to calibrate.

2. MODEL FORMULATION

The model formulation for PM4Silt follows directly from the stress-ratio controlled, critical state based, bounding-surface plasticity formulation for the PM4Sand model (version 3.1), which is fully described in Ziotopoulou and Boulanger (2016) and Boulanger and Ziotopoulou (2017). The PM4Sand model was based on the framework of the bounding surface plasticity (Dafalias 1986) model by Dafalias and Manzari (2004), with subsequent modifications to improve its ability to represent behaviors important to earthquake engineering applications. Modifications in PM4Silt relative to PM4Sand include: (1) the critical state line is linear in void ratio (e) versus logarithm of mean effective stress (p) space instead of curved, and the state parameter (ξ) is utilized instead of the relative state parameter index, (2) the shear modulus is proportional to p raised to a power n_G rather than a power of 0.5, (3) the bounding surface relationship has different forms for both loose (wet) and dense (dry) of critical state conditions, (4) the dilatancy relationship has different forms for both dilation and contraction to allow for more direct control of excess pore pressure generation during cyclic undrained loading. The PM4Sand and PM4Silt models are currently limited to plane-strain applications because their present implementations were simplified by casting the various constitutive relationships in terms of the in-plane stresses only, which is not applicable for general cases but has the advantage of improving computational speed. The constitutive equations for PM4Sand and PM4Silt are listed together in Table A1 to illustrate their common features and areas of difference.

Only those aspects of the PM4Silt model formulation that differ from the PM4Sand formulation are described herein; all constitutive equations and solution procedures are listed in Table A1 for reference, but readers unfamiliar with the general formulation and solution procedures are referred to earlier publications for detailed explanations.

The numerical implementation of PM4Silt as a dynamic link library for use in the explicit finite difference program FLAC 8.0 (Itasca 2016) is identical to that for PM4Sand, as previously described in Ziotopoulou and Boulanger (2013). The PM4Silt model is particularly suited for an explicit implementation that does not require evaluation of the consistent tangent operator. Simulation examples indicate that consistent results are obtained with strain increments of about 10^{-6} or smaller (Boulanger and Ziotopoulou 2018). This constraint on strain increment sizes is generally satisfied in dynamic analyses involving saturated soils with the default time step criteria in FLAC, but sensitivity of system-level simulation results to the dynamic time step should always be evaluated. The manual, dynamic link library, and example calibration files for PM4Silt are available at pm4silt.engr.ucdavis.edu.

Dilation and bounding stress ratios

The model incorporates yield, bounding, dilation, and critical state surfaces, as schematically illustrated in Figure 1, following the basic framework of Dafalias and Manzari (2004). Yielding is stress ratio based, with the deviatoric stress ratio tensor $\mathbf{r}$ equal to the deviatoric stress tensor $\mathbf{s}$ normalized by the mean effective stress (p), where $\mathbf{s}$ is equal to the stress tensor $\boldsymbol{\sigma}$ minus p times the identity tensor. Note that the conventional prime symbol may be dropped from stress terms for convenience since the model is based only on effective stresses. The back-stress ratio tensor $\boldsymbol{\alpha}$ defines the center of the yield surface, which is a small cone of radius m in stress space for a fixed value of the state parameter (ξ) (Been and Jefferies 1985). The model is then formulated in terms of back-stress ratios, including the kinematic hardening and the image back-stress ratio tensors for the dilatancy surface ($\boldsymbol{\alpha}^{\mathbf{d}}$) and the bounding surface ($\boldsymbol{\alpha}^{\mathbf{b}}$). The absolute values of $\boldsymbol{\alpha}^{\mathbf{d}}$ and $\boldsymbol{\alpha}^{\mathbf{b}}$ are set by the dilation stress ratio (M^d) and bounding stress ratio (M^b), respectively. The M^d and M^b values are functions of ξ, as described below, such that they move together during shearing until they

coincide with the critical state surface when the soil has reached critical state. The critical state line is taken to be linear in void ratio (e) versus natural logarithm of p space with slope λ.

The M^d is related to the critical state stress ratio (M) by the expression,

$$M^d = M \cdot \exp\left(n^d \xi\right) \tag{1}$$

where the model parameter n^d is a positive number so that M^d is smaller than M for dense of critical states and greater than M for loose of critical states. The value of M is equal to $2\sin(\phi_{cv})$, where ϕ_{cv} is the critical state friction angle, because the present formulation is limited to plane-strain conditions and assumes the yield surfaces are independent of Lode angle.

The M^b has different forms for dense versus loose of critical states. For loose of critical states (i.e., the "wet" side), M^b is related to M by the expression,

$$M^b = M \cdot \exp\left(-n^{b,wet} \xi\right) \tag{2}$$

where the model parameter $n^{b,wet}$ is a positive number so that M^b is smaller than M for loose of critical states. For dense of critical states (i.e., the "dry" side), M^b is related to M by the expression,

$$M^b = M \cdot \left(\frac{1 + C_{Mb}}{\frac{p}{p_{cs}} + C_{Mb}} \right)^{n^{b,dry}} \tag{3}$$

$$C_{Mb} = \frac{1}{\left(\frac{M^{b,\max}}{M} \right)^{1/n^{b,dry}} - 1} \tag{4}$$

$$M^{b,\max} = 2 \cdot \sin\left(\phi_{\max}\right) \tag{5}$$

where p_{cs} is the p at critical state for the current e, and the model parameter $n^{b,dry}$ is a positive number such that M^b is always larger than M because $p/p_{cs} < 1$ for dense of critical states. The above expression produces M^b values that smoothly vary from equal to M at critical state (i.e., p/p_{cs}

= 1) to a maximum value $M^{b,max}$ at the origin (i.e., $p = 0$). The value of $M^{b,max}$ corresponds to the maximum friction angle than can be mobilized near the origin, ϕ_{max}. A default fixed value of ϕ_{max} = 60 degrees was selected because it provided reasonable bounds for cyclic stress paths near the origin as observed in tests on various fine-grained soils, and the small effects of this parameter on the model calibration and responses did not warrant greater refinement.

For soil at a fixed value of ξ (with corresponding fixed values for p/p_{cs}, M^d, and M^b), the bounding, dilatancy, and critical stress ratio surfaces can be visualized as linear lines on a *q-p* plot (where $q=\sigma_1-\sigma_3$) as shown in Figure 1. As noted previously, the values of M^b and M^d will both approach the value of M as the model is sheared toward critical state ($\xi = 0$, $p/p_{cs} = 1$).

For a soil at a fixed value of e, the locus of points on the bounding surface in a *q-p* plot will be curved because changes in p will correspond to changes in ξ and M^b. This is illustrated in Figure 2 showing q/p_{cs} versus p/p_{cs} for points on the bounding surface for soil at a fixed e. For loose of critical states (i.e., $p/p_{cs} > 1$), the locus of *q-p* points on the bounding surface becomes flat for $n^{b,wet}$ = 1.0 and becomes steeper with decreasing values of $n^{b,wet}$ until it follows M at the limit of $n^{b,wet}$ = 0.0. For dense of critical states (i.e., $p/p_{cs} < 1$), the concave locus of *q-p* points on the bounding surface is stretched outward for larger values of $n^{b,dry}$ and pulls closer to M with decreasing values of $n^{b,dry}$. The functional forms for M^b, as illustrated in this figure, are later shown to be important for controlling undrained (i.e., constant void ratio) behaviors in monotonic and cyclic loading.

Dilatancy and dilation

The dilatancy (D) is defined as the ratio of the plastic volumetric strain increment to the plastic deviatoric strain increment. The dilatancy is non-associative and becomes negative (i.e., produces negative plastic volumetric strain increments or dilation during shearing) for either: (1) continued shearing at stress ratios exceeding M^d, or (2) continued shearing at p less than $2p_{min}$, where p_{min} is

an internal model parameter. The first criterion is the same as utilized in the PM4Sand model, whereas the second criterion is added to control the maximum excess pore pressure that is generated during cyclic undrained shearing. For $p < 2p_{min}$, the value of D is constrained to be less than or equal to:

$$D = -3.5A_{do}\left\langle M^b - M^d \right\rangle \frac{2p_{\min} - p}{p_{\min}} \quad for \quad p_{\min} \le p \le 2p_{\min} \tag{6}$$

The model parameter A_{do} defaults to a value of 0.8, which ensures an approximate consistency with the stress-dilatancy relationships developed by Rowe (1962) and Bolton (1986) for sands. These stress-dilatancy relationships were considered a reasonable starting point for constraining A_{do} for very low plasticity silts, while recognizing that future studies may justify varying A_{do} based on the soil characteristics. The MacCauley brackets $\langle\rangle$ set negative arguments to zero. This expression ensures that, for dense of critical soils (i.e., $M^b > M^d$), the model will cease to be contractive at $p = 2p_{min}$ and become dilative for $p < 2p_{min}$.

The parameter p_{min} is set in one of two ways. One way is for the user to specify a value for the input parameter $r_{up,max}$ (analogous to, but not to be confused with, the excess pore pressure ratio r_u commonly defined relative to initial vertical effective stress). If a value for $r_{up,max}$ is specified, then p_{min} is computed from the value of p at the time of "consolidation" (i.e., the p value when the model is initialized or the command to re-initialize is given) as:

$$p_{\min} = \left(1 - r_{up,\max}\right)\frac{p}{2} \tag{7}$$

The parameter $r_{up,max}$ is limited to a maximum value of 0.99 and a minimum value of zero. For example, setting $r_{up,max}$ equal to 0.95 results in p_{min} and $2p_{min}$ being 2.5% and 5% of the value of p at consolidation, respectively. If $r_{up,max}$ is not specified, p_{min} is set equal to $p_{cs}/8$, where p_{cs} is the value of p at critical state for the specified $s_{u,\mathrm{cs}}$. This default relation can be expressed as,

$$p_{\min} = \frac{p_{cs}}{8} = \frac{2s_{u,cs}}{8M} \tag{8}$$

The p_{min} obtained from this expression would, for example, be equivalent to that obtained by setting the parameter $r_{up,max}$ = 0.84 (for use in Equation 7) for a case with $s_{u,cs}/\sigma'_{vc}$ = 0.25, M = 1.05, and the coefficient of lateral earth pressure at rest K_o = 0.5. In addition, the p_{min} value obtained using this expression is limited to be: (1) no greater than the p_{min} computed using $r_{up,max}$ = 0, which corresponds to the case where cyclic loading will not generate excess pore pressures, and (2) to be no smaller than 0.5 kPa to avoid numerical issues that would develop at zero effective stress. Lastly, maximum pore pressures generated in single element simulations of cyclic undrained loading will actually be limited by $2p_{min}$ because that is where the model ceases to be contractive; the inclusion of dilation at $p < 2p_{min}$ can become active under the more general loading conditions in system level analyses.

Dilatancy and contraction

The dilatancy during contraction (i.e., positive plastic volumetric strain increments) is computed as,

$$D = A_{dc} \cdot \left[\left(\boldsymbol{\alpha} - \boldsymbol{\alpha}_{in}^{app} \right) : \boldsymbol{n} + C_{in} \right]^2 \frac{\left(\boldsymbol{\alpha}^d - \boldsymbol{\alpha} \right) : \boldsymbol{n}}{\left(\boldsymbol{\alpha}^d - \boldsymbol{\alpha} \right) : \boldsymbol{n} + C_D} C_{p\min} \tag{9}$$

$$A_{dc} = \frac{A_{do} \left(1 + \langle \boldsymbol{z} : \boldsymbol{n} \rangle \right)}{h_p C_{dz} C_{wet}} \tag{10}$$

$$C_{wet} = \frac{1}{\dfrac{1}{1 + \left(\dfrac{C_{w1}}{\left(\alpha^b - \alpha \right) : \mathrm{n}} \right)^4} + \dfrac{1}{1 + \left(\dfrac{\xi / \lambda}{C_{w2}} \right)^2}} \leq 1 \tag{11}$$

$$C_{w1} = 0.02 \tag{12}$$

$$C_{w2} = 0.1 \tag{13}$$

$$\begin{aligned} C_{p\min} &= 0 \quad for \quad p < 2p_{\min} \\ &= 1 \quad for \quad p > 8p_{\min} \\ &= \frac{p - 2p_{\min}}{6p_{\min}} \quad otherwise \end{aligned} \tag{14}$$

The initial apparent back-stress ratio tensor ($\boldsymbol{\alpha}_{in}^{app}$) is the value of $\boldsymbol{\alpha}$ at the start of the current loading path (i.e., since the last loading reversal), subject to adjustments (Ziotopoulou and Boulanger 2016) to avoid the over-stiffening associated with small loading reversals in traditional bounding surface models (e.g., Kan and Taiebat 2014). The bounding and dilation image back-stress ratio tensors $\boldsymbol{\alpha}^b$ and $\boldsymbol{\alpha}^d$ define the center of the yield surface if it were contacting the bounding or dilation surfaces at the image points computed for the current tensor **n** normal to the yield surface (Dafalias 1986, Dafalias and Manzari 2004). The fabric tensor **z** evolves in response to plastic deviatoric shear strains and is used to account for prior plastic straining. The parameter A_{dc} for contraction is related to the value of A_{do} for dilation by dividing it by the contraction rate function h_p that can be varied during the calibration process to obtain desired cyclic resistance ratios. The effect of varying states on cyclic loading behavior was then conveniently incorporated by making h_p depend on ξ/λ as follows.

$$h_p = h_{po} \cdot \exp\left(-0.7 + 0.2 \left\langle 3 - \frac{\xi}{\lambda} \right\rangle^2 \right) \tag{15}$$

Thus, the scalar constant h_{po} provides a linear scaling of contraction rates while the functional form of the remaining portion of this expression provides for stronger variations with state parameter (which helps with calibration of the h_{po} values). The variation of h_p with ξ/λ for different values of h_{po} is plotted in Figure 3. Once the other input parameters have been selected, the constant h_{po} can be calibrated to arrive at a desired cyclic resistance ratio.

The factors C_{in}, C_{pmin}, and C_{wet} each constrain or modify D for specific loading conditions. The factor C_{in} depends on the fabric tensor **z**; C_{in} is zero for unfavorable fabric (**z**:**n** < 0), and increases with increasing **z**:**n** for favorable fabric to enhance the contraction rate at the start of an unloading cycle (note that D would be zero at the start of an unloading cycle if C_{in} was zero). The factor C_{pmin} causes the contraction rate to smoothly decrease with decreasing p until D becomes zero when $p = 2p_{min}$. Thus, C_{pmin} provides a smooth transition to the dilation that develops if p drops below 2 p_{min}, as described in the previous section. The term C_{wet} in the denominator of the expression for A_{dc} serves to increase the relative rate of contraction for soils that are only slightly loose of critical state (i.e., small ξ/λ values). This term equals unity when the soil is on the bounding surface, and becomes increasingly smaller than unity for combinations of decreasing ξ (rate controlled by the constant C_{w2}) and increasing distance from the bounding surface (rate controlled by the constant C_{w1}). The constants C_{w1} and C_{w2} have been set to 0.02 and 0.1 because these values produced reasonable responses for a range of calibrations.

Other model components

The remaining components of PM4Silt are the same as for PM4Sand, including the details for the yield criterion, plastic modulus, fabric tensor, hardening coefficient, and loading index. As noted previously, the expressions for each of these components are listed in Table A1, with detailed explanations and background provided in the referenced publications.

3. MODEL INPUT PARAMETERS

The model parameters are grouped into a set of three primary parameters (three required soil parameters), a set of 18 secondary parameters, and a set of six optional analysis control parameters. Default values are provided for all but the three primary parameters, which are the minimum

required inputs for model calibration. The secondary parameters may warrant adjustment from their default values if site-specific laboratory test data are available for calibration.

Primary input parameters

The three primary input parameters are the soil's undrained shear strength at critical state under earthquake loading ratios ($s_{u,cs,eq}$) (or the corresponding undrained shear strength ratio $s_{u,cs,eq}/\sigma'_{vc}$), the shear modulus coefficient G_o, and the contraction rate parameter h_{po}. These parameters are discussed below and summarized in Table 1.

The first required soil parameter is the s_u that corresponds to critical state conditions (i.e., $s_{u,cs}$) at the strain rate expected during earthquake shaking; additional subscripts will be used to differentiate between the strengths expected at earthquake loading rates ($s_{u,cs,eq}$) versus static loading rates ($s_{u,cs,static}$), with the distinction being important for deciding which value of $s_{u,cs}$ should be input to the constitutive model. The s_u of clays and plastic silts can be estimated in practice by a combination of in-situ testing (e.g., cone penetration tests, vane shear tests), laboratory testing of "undisturbed" field samples (e.g., consolidated undrained triaxial or direct simple shear tests), and empirical correlations for undrained shear strength ratio versus over-consolidation ratio (e.g., Ladd and DeGroot 2003). The undrained stress-strain response at strains greater than a few percent can range from strain-hardening for highly over-consolidated soils (i.e., dense of critical) to strain-softening for normally consolidated or lightly over-consolidated soils (i.e., loose of critical). In addition, the s_u is generally rate dependent (e.g., Sheahan et al. 1996) such that the shear resistance during earthquake loading can be 20-40% greater than measured in standardized laboratory tests that use far slower loading rates (e.g., Boulanger and Idriss 2007). The peak s_u produced by PM4Silt can be greater than $s_{u,cs}$ if the other input parameter selections (particularly the combination of $n^{b,wet}$ and h_{po}) produce post peak strain-softening behavior, as illustrated later.

Alternatively, the $s_{u,cs}$ value can be initialized by specifying an undrained shear strength ratio ($s_{u,cs}/\sigma'_{vc}$) that is used to compute $s_{u,cs}$ from the σ'_{vc} at "consolidation" (i.e., at the time of model initialization or whenever the model is reinitialized by resetting the parameter FirstCall to zero). If the user inadvertently specifies values for both $s_{u,cs}$ and $s_{u,cs}/\sigma'_{vc}$, the value of $s_{u,cs}$ is used.

The value specified for $s_{u,cs}$ is used internally to compute the critical state line intercept e_{1kPa}, conditional on the other input parameters, at the time of model initialization,

$$e_{1kPa} = e_o + \lambda \cdot \ln\left(\frac{2 \cdot s_{u,cs}}{M}\frac{101.3kPa}{P_A}\right) \tag{16}$$

where e_o is the current void ratio and P_A is atmospheric pressure. Note that the model requires the numerical value of P_A be specified to establish the unit set being used in the analyses (e.g., 1 atm, 101.3 kPa), and that $s_{u,cs}$ be expressed in the same unit set as P_A. In some sense, $s_{u,cs}$ is not a constitutive model parameter, but rather an input parameter that is used to compute the model parameter e_{1kPa} that positions the critical state line to ensure the model produces the desired $s_{u,cs}$ during subsequent undrained shearing (Figure 4). For this reason, the monotonic undrained and cyclic loading responses are generally insensitive to variations in e_o, λ or ϕ. The model does not currently account for any anisotropy in $s_{u,cs}$ values; the peak s_u will exhibit some loading path dependence, but the user must select s_u to be consistent with the expected mode of deformation in the structure being analyzed.

The second required soil parameter is the constant G_o that controls the elastic (or small strain) shear modulus as,

$$G_{max} = G_o p_A \left(\frac{p}{p_A}\right)^{n_G} \tag{17}$$

The elastic shear modulus can be calibrated to fit in-situ V_s measurements, according to,

$$G_{max} = \rho \cdot \left(V_s\right)^2 \tag{18}$$

or alternatively fit to values of V_s that may be estimated by correlations (e.g., Carlton and Pestana 2016). The shear modulus exponent n_G has a default value of 0.75, but may be adjusted as warranted.

The remaining third required soil parameter is the constant h_{po} that is used to modify the contractiveness and hence enable calibration of the model to specific values of the cyclic resistance ratio (*CRR*). The target *CRR* values for clays and silts with PIs greater than about 7 can be expressed as a cyclic strength ratio, wherein the cyclic strength is expressed as a ratio of the monotonic s_u as illustrated in Figure 5 for a set of natural silts and clays (Boulanger and Idriss 2007). These relationships are intended for the range of loading rates expected during earthquakes, recognizing that the cyclic strength for low plasticity silts and clays exhibit a strain-rate dependence comparable to that observed for s_u (e.g., Lefebvre and LeBouef 1987, Zergoun and Vaid 1994, Lefebvre and Pfendler 1996, Boulanger et al 1998). These relationships indicate that the cyclic stress ratio to cause a peak shear strain of 3% in 30 uniform load cycles at earthquake loading rates is about 70-90% of the soil's $s_{u,cs,static}/\sigma'_{vc}$ (e.g., Figure 5) or about 55-70% of the soil's $s_{u,cs,eq}/\sigma'_{vc}$ (allowing for $s_{u,cs,eq}$ being greater than $s_{u,cs,static}$ due to rate effects) for soils with a PI greater than about 7; thus, h_{po} should be calibrated based on the latter range because the s_u being input to the model corresponds to the $s_{u,cs,eq}$ for the strong shaking portion of the dynamic analysis. The cyclic strength ratios or cyclic resistance ratios for younger and lower plasticity fine-grained soils can be lower than shown in Figure 5 (e.g., Dahl 2011), and thus soil-specific laboratory testing can be warranted when the seismic response is sensitive to these ratios.

Secondary input parameters

Secondary input parameters include model parameters for which default values have been developed that will generally produce reasonable behaviors (Table 1). Default values for secondary model parameters can serve as a starting point for parametric analyses if no advanced laboratory test data are available, or as a starting point for more refined calibrations when advanced laboratory test data are available. Responses from single element simulations of monotonic and cyclic undrained loading using these default values are provided in Boulanger and Ziotopoulou (2018) for cases with $s_{u,cs}/\sigma'_v$ of 0.25, 0.5, and 0.75 at various overburden stresses and initial static shear stress ratios.

The secondary model parameters that are most likely to warrant adjustment from their default values will depend on the nature of the soil's responses in site-specific laboratory testing. Experience suggests that the parameters $n^{b,wet}$, $r_{up,max}$, h_o, C_ε, and C_z, are often the most effective in improving site-specific calibrations, while the parameters z_{max}, C_{GD}, and $C_{k\alpha}$ can also be effective in certain situations. Use of these parameters is illustrated later by the example calibrations against soil-specific laboratory test data.

Optional analysis control parameters

An additional six parameters activate or control optional features of the model for convenience in system level analyses within the FLAC platform. The flag *FirstCall* re-initializes the model by setting the back-stress ratio history terms to the current stress ratio, erases all fabric terms, and sets $s_{u,cs}$ based on the current stress state if the option to specify an undrained strength ratio was used. The optional undrained shear strength scaling parameter F_{su} provides a pragmatic means to examine how the post-strong shaking stability of a boundary value problem may be impacted by the slower strain rates associated with static stability (i.e., $s_{u,cs,static}$ versus $s_{u,cs,eq}$) plus any shaking-

induced strength losses not explicitly captured by the constitutive model. When F_{su} is specified, the critical state line is repositioned so the undrained shear strength become equal to F_{su} times the initially specified value for $s_{u,cs}$. A value for F_{su} can be specified at any time, but the intended use is for it to be set at the end of strong earthquake shaking, after which the dynamic analysis should be continued for sufficient time to evaluate post-shaking stability. The effect of F_{su} on the undrained monotonic loading response is illustrated in Figure 6 for $s_{u,cs,eq}/\sigma'_{vc}$ = 0.25 and σ'_{vc} = 1.0 atm. The soil was sheared to 10% shear strain with F_{su} at its default value of 1.0. Values of F_{su} = 0.8, 0.5, and 0.2 were specified at that point, after which undrained shearing continued to 20% shear strain. The responses show that once F_{su} has been specified, the soil strain-softened toward its new critical state undrained strength. The optional post-strong shaking reconsolidation flag *PostShake* and parameter C_{GC} provide a pragmatic means to improve the simulation of reconsolidation volumetric strains after the end of strong shaking. The parameters cr_{hg} and c_{hg} provide optional hour-glassing controls that can be helpful if the calibrated model can approach effective stresses close to zero. These six optional parameters are not applicable to the calibration process or the examples presented herein. Further details on their use are provided in Boulanger and Ziotopoulou (2018).

4. CALIBRATION PROCESS AND EXAMPLES

Calibration process

The approach used to calibrate PM4Silt will depend on the available site characterization and laboratory testing data, as well as on the nature of the system being analyzed. A recommended sequence of steps for calibration are listed below, although alternative approaches may be more efficient in other situations.

[1] Select the undrained shear strength ($s_{u,cs}$) or undrained shear strength ratio ($s_{u,cs}/\sigma'_{vc}$) for critical state conditions (i.e., large strains) and the strain rate of interest (i.e., static or earthquake loading rates).

[2] Select the shear modulus coefficient (G_o) to match the small-strain shear modulus (G_{max}) obtained from estimated or measured shear wave velocities.

[3] Select values for any secondary parameters that can be informed by soil-specific test data, such as n_G, e_o, λ, and ϕ'_{cv}.

[4] Perform single-element simulations of monotonic undrained loading response. If the soil is initially loose of critical state, use $n^{b,wet}$ to adjust the peak s_u as desired.

[5] Perform single-element simulations of cyclic undrained loading at different strain amplitudes and use h_o to adjust, as desired, the dependence of secant shear moduli and equivalent damping ratios on cyclic shear strain amplitude.

[6] Perform single-element simulations of cyclic undrained loading with uniform cyclic stress ratios and use h_{po} to adjust the simulated curve for *CRR* versus number of uniform loading cycles to cause a peak shear strain of 3% (or other preferred failure criterion). In the absence of laboratory test data, the target cyclic strength curve may be estimated based on empirical curves for τ_{cyc}/s_u (e.g., Figure 5) with appropriate adjustments for strain-rate effects.

[7] Examine the stress-strain and stress path responses of the above cyclic loading simulations, and use other secondary parameters such as C_z, C_ε, and $r_{up,max}$ to adjust the shear strain accumulation rate and other features of behavior.

[8] Repeat steps [4] through [7] until no further revisions to input parameters are warranted.

The above calibration process typically requires only two to four iterations, depending on how close the first trial (with mostly default secondary parameters) approximates the available laboratory test data or target behaviors for sensitivity studies.

Model responses should be examined for any other loading paths that are expected to be important to the system level response. For example, it would be appropriate to plot the stress-strain responses for cyclic loading with a range of overburden stresses and initial static shear stress ratios representative of those expected in the field.

The final calibration should be thoroughly documented in any nonlinear dynamic analysis study, as the documentation is important for facilitating reviews, promoting best practices, and facilitating future reexaminations of seismic performance in practice (Boulanger and Beaty 2016). This documentation should include the results of the single element simulations described in the above calibration process, and any other loading paths expected to be important to the system level response.

Examples of adjustments for key responses

The nature of typical adjustments that might be made in calibration steps 4 (monotonic loading), 5 (modulus reduction and damping), 6 (cyclic strength), and 7 (strain accumulation during cyclic loading) are illustrated in the following examples.

The effects of varying $n^{b,wet}$ or $s_{u,cs}/\sigma'_{vc}$ on the monotonic undrained direct simple shear (DSS) response for a soil that is loose of critical are shown in Figures 7a-7d. The stress-strain and stress path results in Figures 7a and 7b correspond to $s_{u,cs}/\sigma'_{vc} = 0.2$ with $n^{b,wet}$ values of 0.2, 0.5, and 0.8. Reducing $n^{b,wet}$ from the default value of 0.8 to 0.2 shifted the bounding line upward (Figure 2) and increased the peak s_u/σ'_{vc} that developed during undrained shearing from about 0.22 to 0.34 (Figure 7a). The stress-strain and stress path results in Figures 7c and 7d correspond to $n^{b,wet} = 0.5$

with $s_{u,cs}/\sigma'_{vc}$ of 0.1, 0.2, and 0.3. Reducing $s_{u,cs}/\sigma'_{vc}$ from 0.3 to 0.1 reduced the peak s_u/σ'_{vc} from about 0.34 to 0.19 and increased the simulated sensitivities (i.e., $s_{u,peak}/s_{u,cs}$) from 1.1 to 1.9.

The effect of varying h_o on the shear modulus reduction and equivalent damping ratio responses are shown in Figure 8 for undrained strain-controlled DSS loading of a soil with $s_{u,cs}/\sigma'_{vc} = 0.25$ and $\sigma'_{vc} = 100$ kPa. The simulations used h_o values of 0.5, 1.0, and 2.0, and included three cycles of loading at each strain level. The secant G/G_{max} and equivalent damping ratios from the third cycle are plotted versus shear strain amplitude in Figures 8b and 8d, respectively. Also shown on these figures are the empirical curves developed by Vucetic and Dobry (1991) for fine-grained soils with PIs of 0, 15, and 30. The simulation results for $h_o = 0.5$, 1.0, and 2.0 are reasonably close to the PI = 0, 15, and 30 curves, respectively, for strain amplitudes less than about 0.1%. The upward shift of the G/G_{max} curves with increasing h_o is accompanied with a downward shift in the equivalent damping ratios, as expected empirically. The stress-strain responses for $h_o = 0.5$ and 2.0 in Figures 8a and 8c, respectively, show how increasing h_o generally results in narrower hysteresis loops for a given cyclic strain amplitude.

The effect of varying h_{po} on the cyclic strength curve for undrained, uniform cyclic DSS loading is shown in Figure 9 for a soil with $s_{u,cs}/\sigma'_{vc} = 0.25$ and $\sigma'_{vc} = 100$ kPa. Increasing h_{po} from 2 to 40 has only a small effect on the number of cycles to failure at a cyclic stress ratio of 0.25 because these strengths are largely controlled by the monotonic $s_{u,cs}$ value. Increasing h_{po} has a larger effect on the number of cycles to failure at lower cyclic stress ratios, as evidenced by a general flatting of the cyclic strength curves with increasing h_{po} (particularly as h_{po} increased from 2 to 10). The slope of the cyclic strength curves can be approximately described by the exponent for a power law fit, with that exponent being about 0.15-0.16 for the simulations with h_{po} of 10 to 40. These slopes are slightly larger than the 0.12-0.15 obtained for the clays and plastic silts shown

in Figure 5, and near the lower range of values observed for nonplastic silty sands and sands (e.g., which increase from about 0.14 for loose sands to about 0.38 for dense sands; Boulanger and Idriss 2015).

The effect of varying $r_{up,max}$ on the stress-strain response to undrained, uniform cyclic stress ratio DSS loading is shown in Figure 10 for a soil with $s_{u,cs}/\sigma'_{vc} = 0.25$. Simulations were performed using $r_{up,max} = 0.70$, 0.84 (default value for this case), and 0.98, and the corresponding h_{po} values were adjusted to 10, 20, and 24, respectively, to maintain similar cyclic strength curves. The stress-strain and stress path responses for $r_{up,max} = 0.7$ in Figures 10a and 10b show thicker hysteretic loops (greater damping ratios) and slower shear strain accumulation rates after peak excess pore pressures have developed. The stress-strain and stress path responses for $r_{up,max} = 0.98$ in Figures 10e and 10f show more strongly pinched hysteretic loops (lower damping ratios) and faster shear strain accumulation rates. The responses for $r_{up,max} = 0.84$ in Figures 10c and 10d are intermediate to the other cases. The hysteresis loops become more pinched with a flatter middle portion as the $r_{up,max}$ value increases because the effective stresses and associated moduli drop to smaller values during each cycle of loading.

Examples from calibrations for three soils using advanced laboratory test data

Example results from calibrations against monotonic and cyclic undrained DSS test data are presented for three normally consolidated, fine-grained soils: (1) a slurry sedimented, silty clay with PI = 20, LL = 42, and USCS classification of CL, (2) a slurry sedimented, clayey silt with PI = 6, LL =22, and USCS classification of ML, and (3) undisturbed tube samples of Fraser River Delta (FRD) silt with PI = 4, LL = 30, and USCS classification of ML. The first two soils were reconstituted, slurry deposited mixtures of nonplastic silica silt with kaolin: 30% silt plus 70% kaolin (denoted 30S70K), and 80% silt plus 20% kaolin (denoted 80S20K), respectively.

Experimental results for these two soils are provided in Price (2018), and details of the calibration are provided in Boulanger et al. (2018). Experimental results for the FRD silt are provided in Sanin and Wijewickreme (2006) and results of simulations using three alternative calibration protocols are provided in Boulanger and Wijewickreme (2019). The three alternative calibration protocols used in Boulanger and Wijewickreme (2019) illustrate the effect of alternative priorities in the calibration process, such as giving priority to matching undrained monotonic DSS test results versus matching an empirical secant G/G_{max} relationship. Results are presented herein for the third calibration protocol, since the results were generally similar for all three alternatives. The above references show comparisons of measured and simulated monotonic undrained DSS tests, cyclic undrained DSS tests, and secant G/G_{max} and equivalent damping ratio relationships. The calibrated input parameters for each soil are listed in Table 1, indicating which of the secondary parameters were adjusted relative to their default values. Examples from these calibration studies are provided herein to illustrate the flexibility of the model in representing different response characteristics.

Measured and simulated cyclic strength curves for the PI = 20 clay, PI = 6 silt, and PI = 4 FRD silt are shown in Figures 11a-11c, respectively. The cyclic strengths near a single loading cycle are approximately proportional to the monotonic $s_{u,cs}/\sigma'_{vc}$ values, which were 0.21, 0.145, and 0.27 for these three soils, respectively. The measured cyclic strength curves were slightly flatter for the two reconstituted soils than for the natural FRD silt, but the simulations were able to approximate all three curves reasonably.

Measured and simulated stress-strain and stress path responses for one of the cyclic DSS tests for each soil are presented in Figures 12-14. The PI = 20 clay (Figure 12) developed a maximum excess pore pressure ratio of about 85%, which was similar to the value obtained in the simulation with the default value for the parameter $r_{up,max}$. The measured rate of shear strain accumulation was

slower than simulated with the default parameters, so C_z and C_ε were reduced to 20 (from the default of 100) and 0.25 (from the default of 0.5), respectively, to improve the simulation results. The PI = 6 silt (Figure 13) developed a maximum excess pore pressure ratio of about 98%, which required specifying a larger value for the input parameter $r_{up,max}$. This helped the stress-strain loops pinch, but the measured rate of shear strain accumulation was greater than simulated with the default parameters, so C_z and C_ε were increased to 150 and 1.0, respectively. The PI = 4 FRD silt (Figure 14) developed maximum excess pore pressure ratios close to about 95%, which also required modifying the input parameter $r_{up,max}$. This helped the simulated stress-strain loops pinch, but the measured rate of shear strain accumulation was this time slower than simulated with the default parameters, so C_z and C_ε were reduced to 30 and 0.25, respectively. The simulated stress paths, and hence pore pressures, for all three soils are reasonably consistent with measured responses, although certain details of the stress paths at lower effective stresses are not recreated well. The simulated stress-strain responses are also reasonably consistent with the measured responses despite the fact these three soils exhibited significantly different combinations of maximum excess pore pressure ratio, hysteresis loop shapes, and shear strain accumulation rates.

Discussion on calibration

The preceding examples examined calibrations for normally consolidated soils using advanced laboratory test data, but the model is equally applicable to over-consolidated soils (e.g., Figure 4) or to applications where advanced laboratory testing data are not available. The latter case relies more heavily on empirical correlations for guiding model calibration, but the general calibration process presented previously is essentially the same. An example of model calibration for a deposit with over-consolidated clay based primarily on cone penetration test and in-situ shear wave velocity data is available in Boulanger et al. (2019).

The model was specifically developed to provide improved seismic modeling capabilities relative to the simpler hysteretic or elastic-plastic constitutive models commonly used in practice, to be flexible enough to approximate the cyclic loading responses of clays through low-plasticity silts, and to be relatively easy to calibrate for practical applications. The utility of the model for these purposes was demonstrated herein, although it is important to recognize that the model cannot simulate a wide range of other clay and plastic silt behaviors (e.g., anisotropy, secondary compression, evolution of s_u with stress and seismic loading history, post-seismic reconsolidation strains) that can be important for other engineering applications.

5. CONCLUDING REMARKS

The PM4Silt plasticity model was developed for representing clays and plastic silts, as opposed to purely nonplastic silts and sands, in geotechnical earthquake engineering applications. The PM4Silt model builds on the framework of the stress-ratio controlled, critical state based, bounding surface plasticity PM4Sand model (version 3.1; Boulanger and Ziotopoulou 2017). The development of PM4Silt emphasized obtaining reasonable approximations of monotonic undrained shear strengths, cyclic shear strengths, and shear modulus reduction and hysteretic damping responses across a range of initial static shear stress and overburden stress conditions. Modifications to the constitutive relationships relative to PM4Sand model included: (1) the model was recast in terms of the state parameter and the critical state line was changed to be linear in void ratio versus logarithm of mean effective stress space, (2) the ability to modify the stress exponent in the elastic shear modulus relationship was added, (3) the bounding surface relationship was modified for both loose (wet) and dense (dry) of critical state conditions, and (4) the dilatancy and contraction rate relationships were modified to allow for more direct control of the maximum excess pore pressure ratio obtained in cyclic undrained loading. The model is stress-ratio based

and therefore not applicable for modeling static consolidation or post-earthquake consolidation problems, including the evolution of undrained strength with seismic loading or consolidation stress history. The current formulation is limited to plane-strain applications. The model was coded as a user defined material in a dynamic link library (DLL) for use with the commercial program FLAC 8.0 (Itasca 2016).

The primary soil parameters are the undrained shear strength ratio (or undrained shear strength), shear modulus coefficient, and contraction rate parameter. The shear modulus coefficient should be calibrated to the measured or estimated in-situ shear wave velocities. The contraction rate parameter should be calibrated to approximate the measured or expected slope of the CRR versus number of uniform loading cycles curve. Secondary parameters were provided with default values that provide a reasonable starting point for sensitivity studies if advanced laboratory test data are not available or for refined calibrations if advanced laboratory testing data are available.

The calibration process and model responses were illustrated by single-element simulations of monotonic undrained and cyclic DSS tests, including comparisons to experimental data for normally consolidated, slurry deposited specimens of a PI = 20 clay and PI = 6 silt and normally consolidated, tube samples of a natural PI = 4 Fraser River Delta silt. The model was shown to provide reasonable approximations of behaviors important to many applications in earthquake engineering and to be relatively easy to calibrate.

ACKNOWLEDGMENTS

The development of PM4Silt progressed under projects for the California Division of Safety of Dams under Contract 4600009523, the Department of Water Resources under Contract 4600009751, and the National Science Foundation under grant CMMI-1635398. Any opinions,

findings, conclusions, or recommendations expressed herein are those of the authors and do not necessarily represent the views of these organizations.

REFERENCES

[] Andersen K, Kleven A, Heien D. Cyclic soil data for design of gravity structures. Journal of the Geotechnical Engineering Div., ASCE, 1988; 114(5): 517-539.

[] Azzouz AS, Malek AM, Baligh MM. Cyclic behavior of clays in undrained simple shear. J. Geotechnical Engineering Div., ASCE, 1989; 115(5): 637-657.

[] Been K, Jefferies MG. A state parameter for sands. Géotechnique 1985; 35(2), 99–112.

[] Bolton MD. The strength and dilatancy of sands. Géotechnique 1986; 36(1): 65–78.

[] Boulanger RW, Beaty MH. Seismic deformation analyses of embankment dams: A reviewer's checklist. Proceedings, Celebrating the Value of Dams and Levees – Yesterday, Today and Tomorrow, 36th USSD Annual Meeting and Conference, United States Society on Dams, Denver, CO, 2016; 535-546.

[] Boulanger RW, Idriss IM. Magnitude scaling factors in liquefaction triggering procedures. Soil Dynamics and Earthquake Engineering, Elsevier, 2015; 79, 296-303, 10.1016/j.soildyn.2015.01.004.

[] Boulanger RW, Idriss, IM. Evaluation of cyclic softening in silts and clays. Journal of Geotechnical and Geoenvironmental Engineering, ASCE, 2007; 133(6), 641-652.

[] Boulanger RW, Meyers MW, Mejia LH, Idriss IM. Behavior of a fine-grained soil during Loma Prieta earthquake. Canadian Geotechnical Journal, 1998; 35, 146-158.

[] Boulanger RW, Munter SK, Krage CP, DeJong JT. Liquefaction evaluation for an interbedded soil deposit: Çark Canal in the 1999 M7.5 Kocaeli earthquake. Journal of Geotechnical and Geoenvironmental Engineering, ASCE, 2019; in press.

[] Boulanger RW, Price AB, Ziotopoulou K. Constitutive modeling of the cyclic loading response of low plasticity fine-grained soils. GSIC 2018, Proc. GeoShanghai 2018 International Conference: Fundamentals of Soil Behaviours, A. Zhou et al. (Eds.), Springer Nature Singapore Pte Ltd., 2018; 1–13, https://doi.org/10.1007/978-981-13-0125-4_1.

[] Boulanger RW, Wijewickreme D. Calibration of a constitutive model for the cyclic loading response of Fraser River Delta Silt. Earthquake Geotechnical Engineering for Protection and Development of Environment and Constructions: Proceedings of the 7th International Conference on Earthquake Geotechnical Engineering, F. Silvestri and N. Moraci (eds), Associazione Geotecnica Italiana, Rome, Italy, ISBN 978-0-367-14328-2, 121-137..

[] Boulanger RW, Ziotopoulou K. PM4Sand (Version 3.1): A sand plasticity model for earthquake engineering applications. Report No. UCD/CGM-17/01, Center for Geotechnical Modeling, Department of Civil and Environmental Engineering, University of California, Davis, CA, 2017; 113 pp.

[] Boulanger RW, Ziotopoulou K. PM4Silt (Version 1): A silt plasticity model for earthquake engineering applications. Report No. UCD/CGM-18/01, Center for Geotechnical Modeling, Department of Civil and Environmental Engineering, University of California, Davis, CA, 2018; 108 pp.

[] Bray JD, Boulanger RW, Cubrinovski M, Tokimatsu K, Kramer SL, O'Rourke T, Rathje E, Green RA, Robertson PK, Beyzaei CZ. U.S.-New Zealand-Japan International Workshop, Liquefaction-induced ground movement effects. PEER Report 2017/02, Pacific Earthquake Engineering Research Center, University of California, Berkeley, CA, 2017; 278 pp.

[] Carlton BD, Pestana JM. A unified model for estimating the in-situ small strain shear modulus of clays, silts, sands, and gravels. Soil Dynamics and Earthquake Engineering, 2016; 88: 345-355, 10.1016/j.soildyn.2016.01.019.

[] Dafalias YF. Bounding surface plasticity. I: Mathematical foundation and hypoplasticity. J. Engineering Mechanics, 1986; 112(9), 966-987.

[] Dafalias YF, Manzari MT, Papadimitriou, AG. SANICLAY: simple anisotropic clay plasticity model. International Journal for Numerical and Analytical Methods in Geomechanics 2006; 30(12):1231–1257.

[] Dafalias YF, Manzari MT. Simple plasticity sand model accounting for fabric change effects. Journal of Engineering Mechanics, ASCE, 2004; 130(6): 622-634.

[] Dahl KR. Evaluation of seismic behavior of intermediate and fine-grained soils. Doctoral dissertation, University of California, Davis, 2011.

[] Hadidi R, Dinsick A, Wahl D, Hu J, Perez A. Characterization and seismic performance evaluation of Bouquet Canyon Dam No. 1. Proc., Performance-based Design in Earthquake Geotechnical Engineering, PBD-III Vancouver, M. Taiebat et al., eds., ISSMGE Technical Committee TC203, 2017; paper 110.

[] Hu C, Liu H. A new bounding-surface plasticity model for cyclic behaviors of saturated clay. Communications in Nonlinear Science and Numerical Simulation, 2015; 22, 101-119, 10.1016/j.cnsns.2014.10.023.

[] Hyodo M, Yamamoto Y, Sugiyama M. Undrained cyclic shear behavior of normally consolidated clay subjected to initial static shear stress. Soils and Foundations, JSSMFE, 1994; 34(4), 1-11.

[] Itasca. FLAC – Fast Lagrangian Analysis of Continua, Version 8.0, Itasca Consulting Group, Inc., Minneapolis, Minnesota, 2016.

[] Kan ME, Taiebat HA. On implementation of bounding surface plasticity models with no overshooting effect in solving boundary value problems. Computers and Geotechnics, 2014; 55, 103-116, 10.1016/j.compgeo.2013.08.006.

[] Ladd CC, DeGroot DJ. Recommended practice for soft ground site characterization: Arthur Casagrande Lecture. Proc., 12th Panamerican Conference on Soil Mechanics and Geotechnical Engineering, Massachusetts Institute of Technology, Cambridge, MA, 2003; Vol. 1, 3-57.

[] Lefebvre G, LeBouef D. Rate effects and cyclic loading of sensitive clays. J. of Geotechnical Engineering, ASCE, 1987; 113(5), 476-489.

[] Lefebvre G, Pfendler P. Strain rate and preshear effects in cyclic resistance of soft clay. Journal of Geotechnical and Geoenvironmental Engineering, ASCE, 1996; 122(1), 21-26.

[] Luque R, Bray JD. Dynamic analyses of two buildings founded on liquefiable soils during the Canterbury Earthquake Sequence. Journal of Geotechnical and Geoenvironmental Engineering, ASCE, 2017; 143(9): 04017067.

[] Naesgaard E. A Hybrid Effective Stress – Total Stress Procedure for Analyzing Soil Embankments Subjected to Potential Liquefaction and Flow. Ph.D. dissertation, University of British Columbia, Vancouver, Canada, 2011.

[] Ni J, Indraratna B, Geng X-Y, Carter JP, Chen YL. Model of soft soils under cyclic loading. International Journal of Geomechanics, ASCE, 2015; 04014067, 10.1061/(ASCE)GM.1943-5622.0000411.

[] Price AB. Cyclic Strength and Cone Penetration Resistance for Mixtures of Silica Silt and Kaolin. Doctoral dissertation, University of California, Davis, 2018.

[] Rampello S, Cascone E, Grosso N. Evaluation of the seismic response of a homogenous earth dam. Soil Dynamics and Earthquake Engineering, 2009; 29, 782-798, 10.1016/j.soildyn.2008.08.006.

[] Rowe PW. The stress-dilatancy relation for static equilibrium of an assembly of particles in contact. Proc. R. Soc. London, Ser. A, 1962; 269: 500-527.

[] Sanin MV, Wijewickreme D. Cyclic shear response of channel-fill Fraser River Delta silt. Soil Dynamics and Earthquake Engineering, 2006; 26: 854-869.

[] Schanz T, Vermeer PA, Bonnier PG. Formulation and verification of the hardening-soil model. Beyond 2000 in computational geotechnics. R. B. J. Brinkgreve, ed. Rotterdam, Balkema, 1999; 281–90.

[] Seidalinov G, Taiebat M. Bounding surface SANICLAY plasticity model for cyclic clay behavior. International Journal for Numerical and Analytical Methods in Geomechanics, 2014; 38: 702-724.

[] Sheahan TC, Ladd CC, Germaine JT. Rate-dependent undrained shear behavior of saturated clay. Journal of Geotechnical Engineering, 1996; 122(2), 99-108.

[] Taiebat M, Dafalias YF, Peek R. A destructuration theory and its application to SANICLAY model. International Journal for Numerical and Analytical Methods in Geomechanics July 2010; 34(10):1009–1040.

[] Tasiopoulou P, Giannakou A, Chacko J, de Wit S. Liquefaction triggering and post-liquefaction deformation of laminated deposits. Soil Dynamics and Earthquake Engineering, 2018; 10.1016/j.soildyn.2018.04.044.

[] Vucetic M, Dobry R. Effect of soil plasticity on cyclic response. Journal of Geotechnical Engineering, 1991; 117(1), 89–107.

[] Woodward-Clyde Consultants. California Water Operations Center – Site Evaluation and Remediation – Conceptual Design. Appendix E: CWOC Site Characterization Memo. Oakland, California, 1992.

[] Yang Z, Lu JL, Elgamal A. OpenSees soil models and solid-fluid fully coupled elements: User's manual, Version 1.0. Department of Structural Engineering, University of California, San Diego, 2008.

[] Zergoun M, Vaid YP. Effective stress response of clay to undrained cyclic loading. Canadian Geotechnical Journal, 1994; 31, 714–727.

[] Ziotopoulou K, Boulanger RW. Calibration and implementation of a sand plasticity plane-strain model for earthquake engineering applications. Soil Dynamics and Earthquake Engineering, 2013; 53, 268-280, 10.1016/j.soildyn.2013.07.009.

[] Ziotopoulou K, Boulanger RW. Plasticity modeling of liquefaction effects under sloping ground and irregular cyclic loading conditions. Soil Dynamics and Earthquake Engineering, 2016; 84 (2016), 269-283, 10.1016/j.soildyn.2016.02.013.

Table 1. Input parameters for PM4Silt example calibrations.

Input parameter [a]	Default value	Calibrated values [b]		
		PI = 20 silty clay	PI = 6 clayey silt	PI = 4 FRD silt [c]
$s_{u,cs}/\sigma'_{vc}$ – s_u at critical state	-- [d]	0.21	0.145	0.27
G_o – shear modulus coefficient	-- [d]	345	736	500
h_{po} – contraction rate parameter	-- [d]	1.2	2.2	25.0
n_G – shear modulus exponent	0.75	1.0	--	0.6
h_o – plastic modulus ratio	0.5	--	--	0.1
e_o – initial void ratio	0.9	1.00	0.61	0.922
λ – compressibility in e-ln(p') space	0.06	0.18	0.07	0.057
ϕ'_{cv} – critical state friction angel	32°	25°	32°	32°
$n^{b,wet}$ – bounding surface parameter	0.8	1.0	--	1.0
$n^{b,dry}$ – bounding surface parameter	0.5	--	--	--
n^d – dilation surface parameter	0.3	--	--	--
A_{do} – dilatancy parameter	0.8	--	--	--
$r_{up,max}$ – sets bounding p_{min}	$p_{min} = p_{cs}/8$	--	0.99	0.95
z_{max} – fabric term	$10 \le 40(s_u/\sigma'_{vc}) \le 20$	--	--	--
C_z – fabric growth parameter	100	20	150	30
C_ε – strain accumulation rate factor	$0.5 \le (1.2s_u/\sigma'_{vc} + 0.2) \le 1.3$	0.25	1.0	0.25
C_{GD} – modulus degradation factor	3.0	--	--	--
$C_{k\alpha f}$ – plastic modulus factor	4.0	--	--	--
ν_o – Poisson ratio	0.3	--	--	--

[a] Excluding the initialization flag FirstCall, the post-shaking undrained strength reduction parameter F_{su}, the post-shaking consolidation flag PostShake and parameter C_{GC}, and the hour-glassing control parameters (cr_{hg}, c_{hg}).

[b] Retained default value if no entry listed.

[c] Third of three alternative calibrations compared in Boulanger and Wijewickreme (2019)

[d] Required input parameter that does not have a default value.

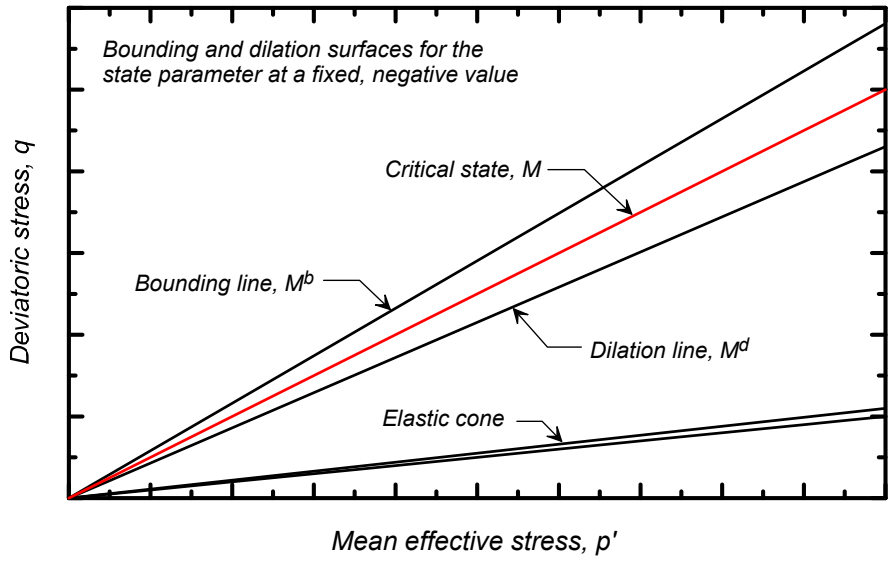

Figure 1. Schematic of the bounding, critical state, and dilation lines in q-p' space for a fixed value of state parameter (for dense of critical state conditions).

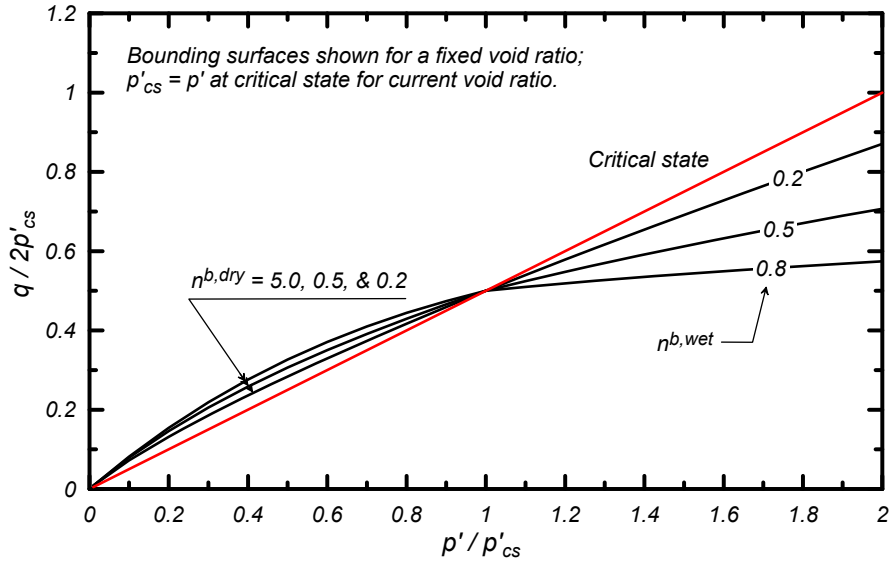

Figure 2. Schematic of the bounding lines and critical state line in q-p' space for a fixed value of void ratio and a range of $n^{b,dry}$ values (for dense of critical state conditions) and $n^{b,wet}$ values (for loose of critical state conditions).

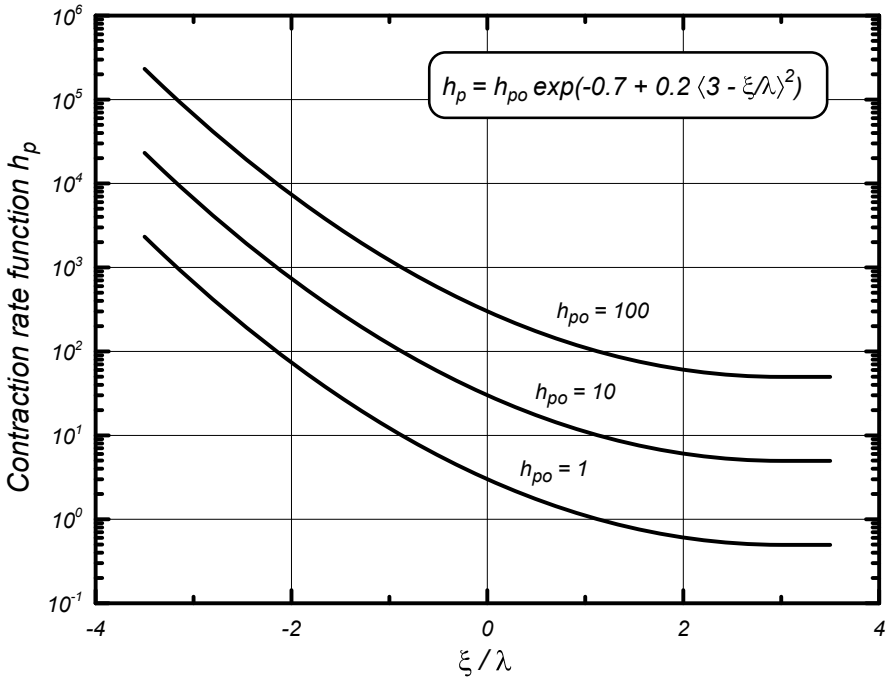

Figure 3. Variation of contraction rate function h_p with ξ/λ and contraction rate parameter h_{po}.

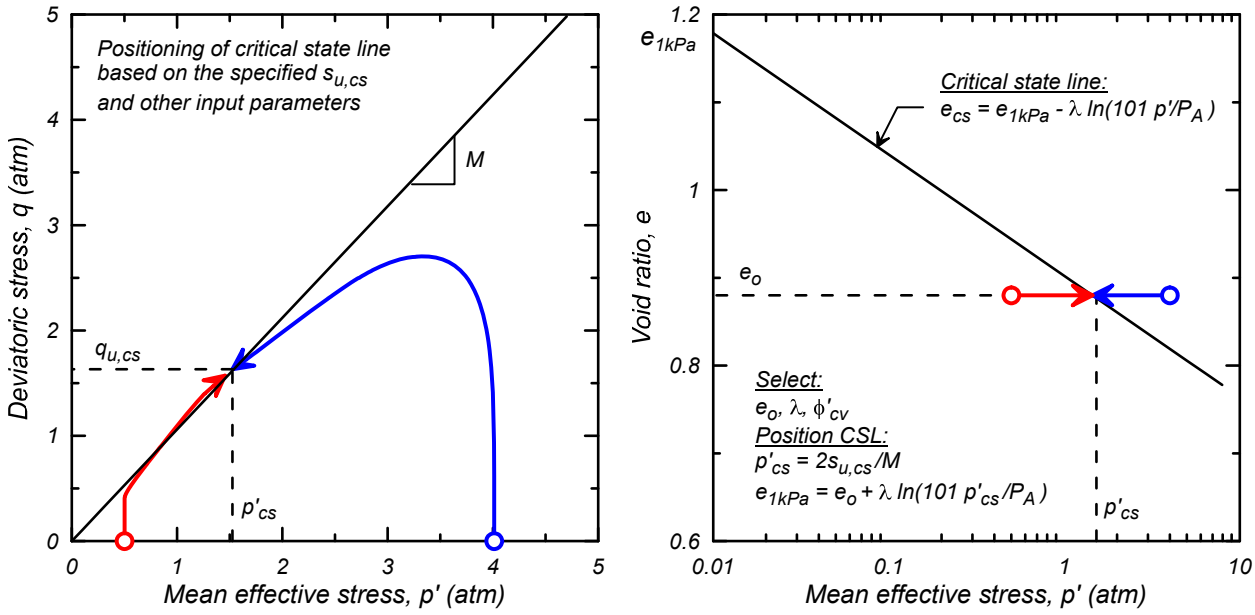

Figure 4. Procedure for positioning the critical state line based on the specified $s_{u,cs}$, along with simulated undrained responses for specimens with the same $s_{u,cs}$ but starting at consolidation stresses corresponding to initially loose and dense of critical state conditions.

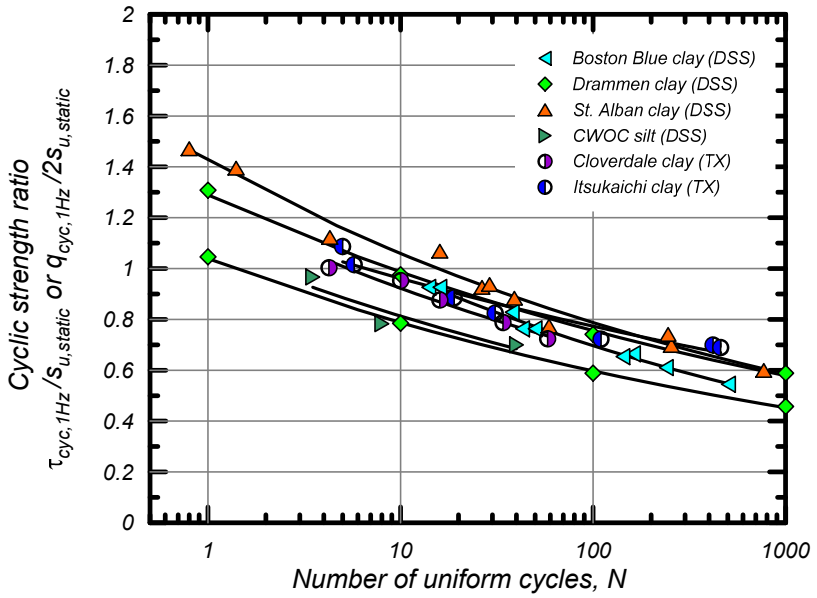

Figure 5. Cyclic strength ratio to cause a peak shear strain of 3% versus number of uniform loading cycles for natural soils with PIs greater than about 7; cyclic stresses at a loading frequency of 1 Hz and monotonic strengths at standard testing rates (from Boulanger and Idriss 2007, with data from Andersen et al. 1988, Azzouz et al. 1989, Hyodo et al. 1994, Lefebvre and Pfendler 1996, Woodward-Clyde 1992, Zergoun and Vaid 1994).

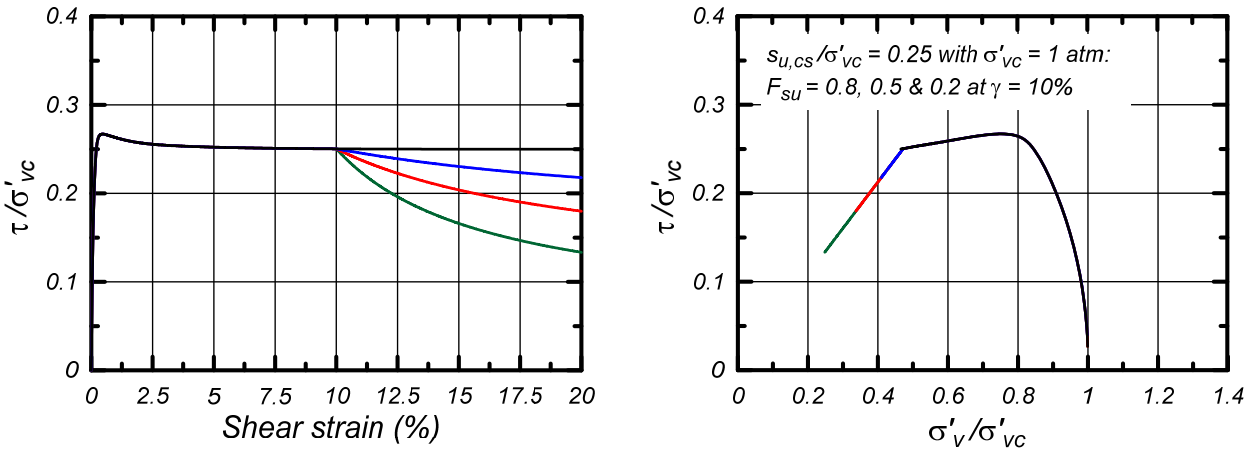

Figure 6. Effect of setting F_{su} = 0.8, 0.5, or 0.2 at γ = 10% on the response to further monotonic undrained DSS loading for a soil with $s_{u,cs}/\sigma'_{vc}$ = 0.25.

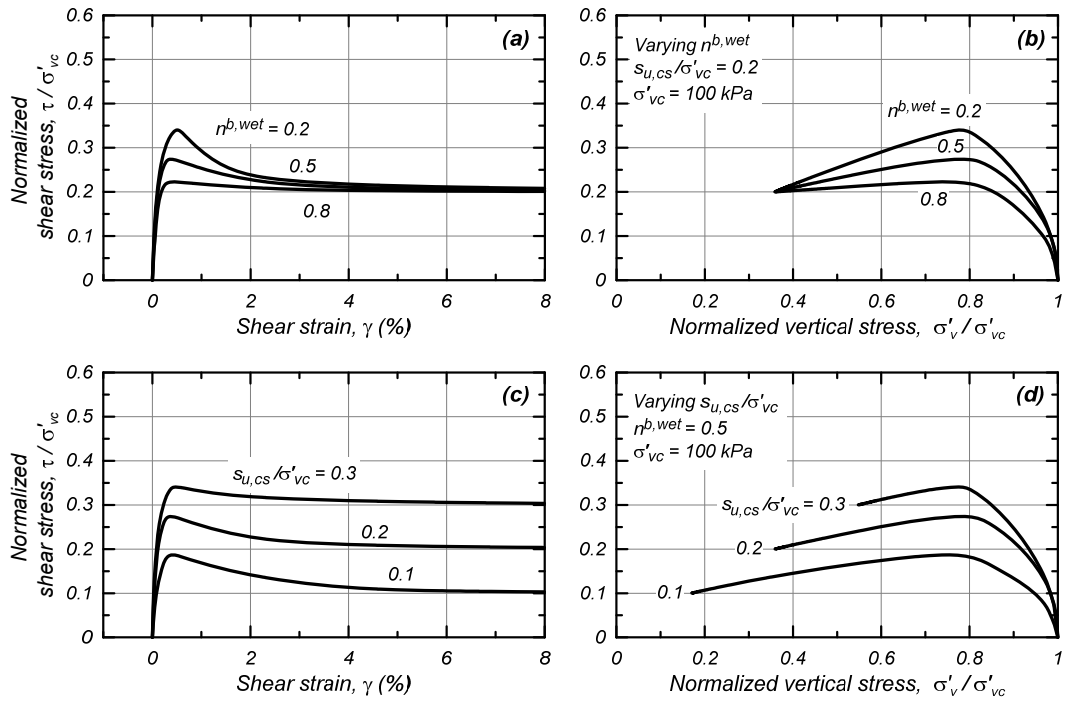

Figure 7. Stress-strain and stress path responses for monotonic undrained DSS loading: (a-b) varying $n^{b,wet}$ with $s_{u,cs}/\sigma'_{vc} = 0.20$, and (c-d) varying $s_{u,cs}/\sigma'_{vc}$ with $n^{b,wet} = 0.5$.

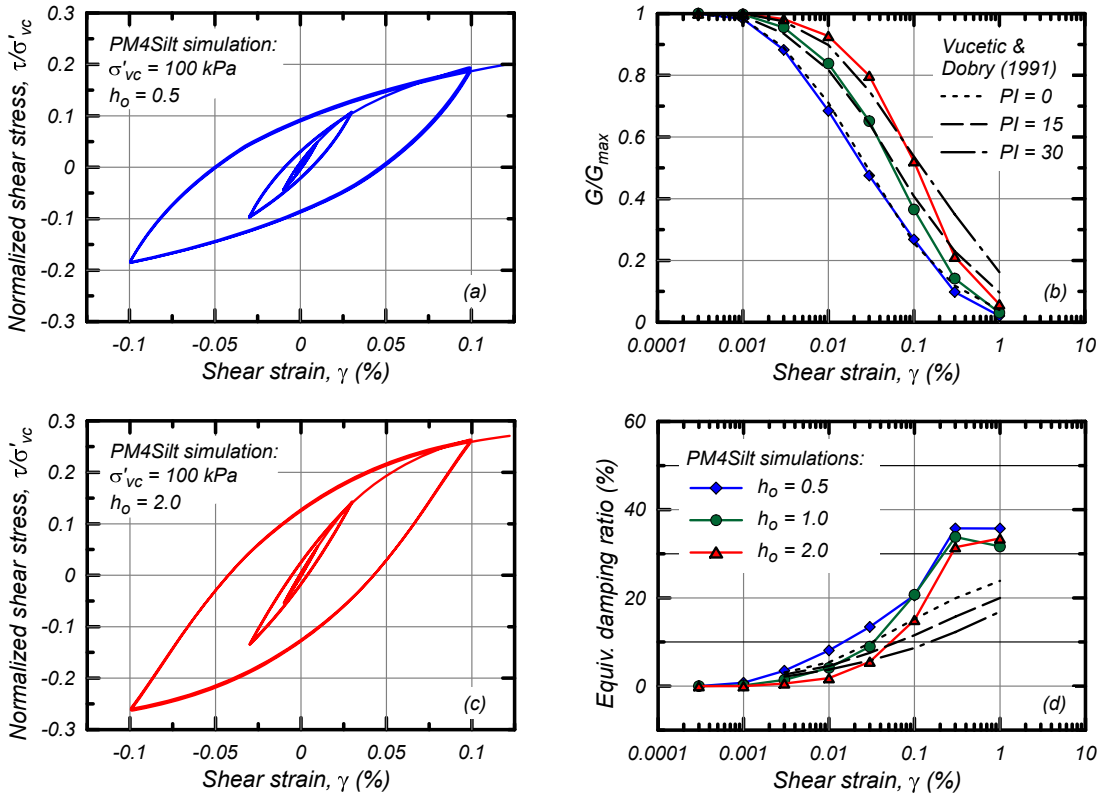

Figure 8. Effect of h_o on the shear modulus reduction and equivalent damping ratios from cyclic undrained strain-controlled DSS loading for baseline parameters with $s_{u,cs}/\sigma'_{vc} = 0.25$.

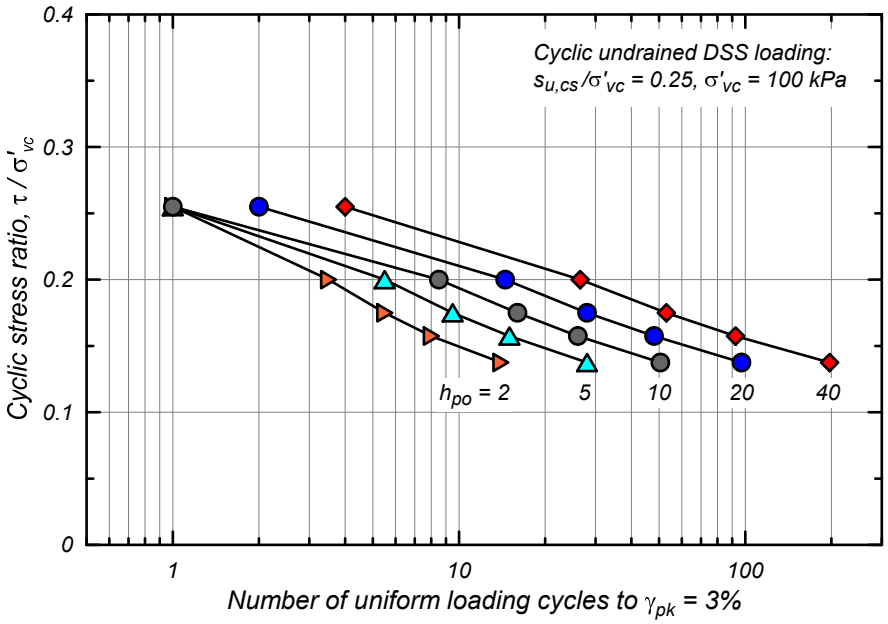

Figure 9. Cyclic stress ratio required to cause a peak shear strain of 3% versus number of equivalent uniform loading cycles for different h_{po} values.

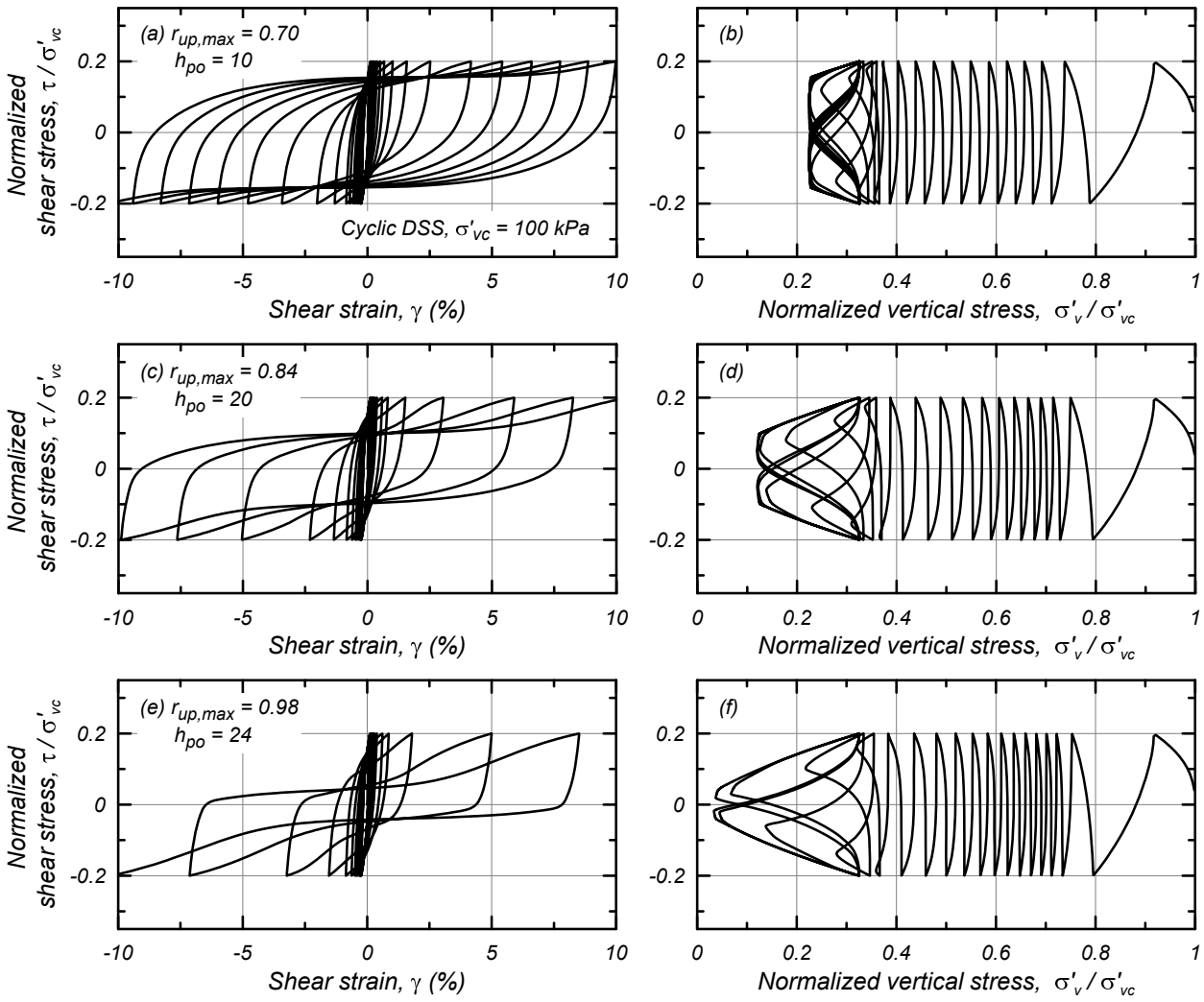

Figure 10. Cyclic mobility responses for cyclic undrained stress-controlled DSS loading with $s_{u,cs}/\sigma'_{vc}$ = 0.25 and different combinations of $r_{up,max}$ and h_{po} that produce comparable cyclic resistance ratios: (a-b) $r_{up,max}$ = 0.7 and h_{po} = 10, (c-d) $r_{up,max}$ = 0.84 and h_{po} = 20, (e-f) $r_{up,max}$ = 0.98 and h_{po} = 24.

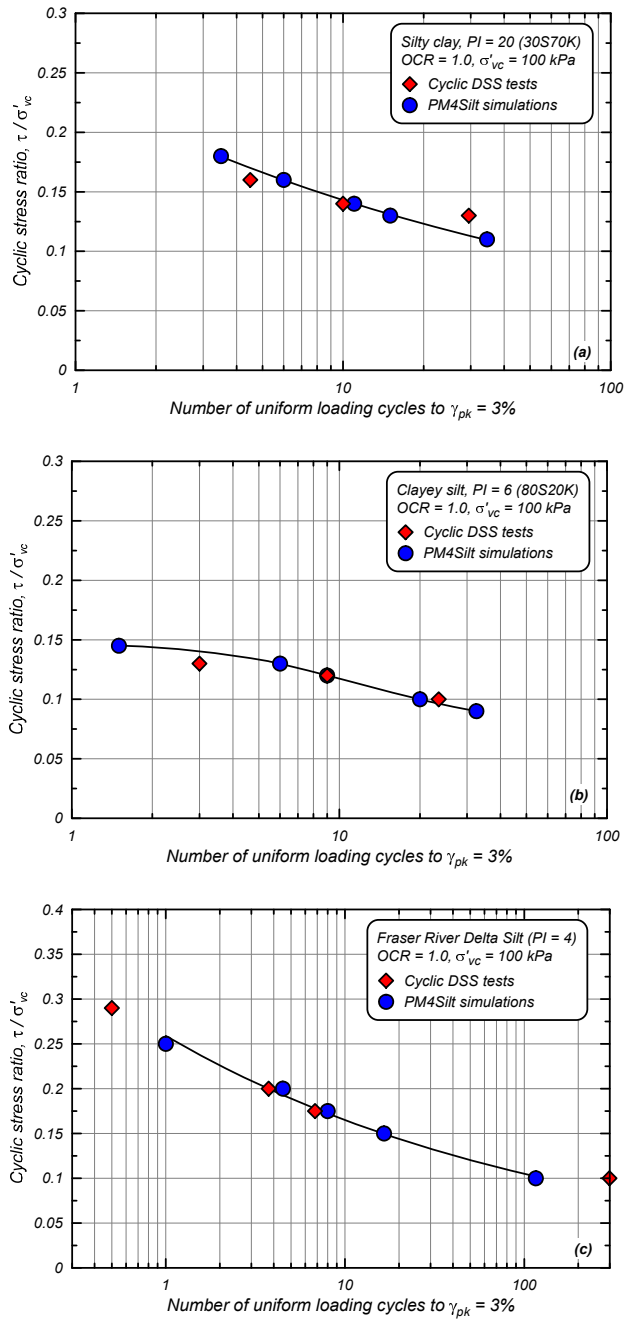

Figure 11. Measured and simulated cyclic strength curves for cyclic undrained DSS loading on three soils: (a) slurry sedimented, normally consolidated silty clay with PI=20, (b) slurry sedimented, normally consolidated clayey silt with PI=6, and (c) high-quality tube samples of Fraser River Delta silt with PI=4 normally consolidated in the laboratory.

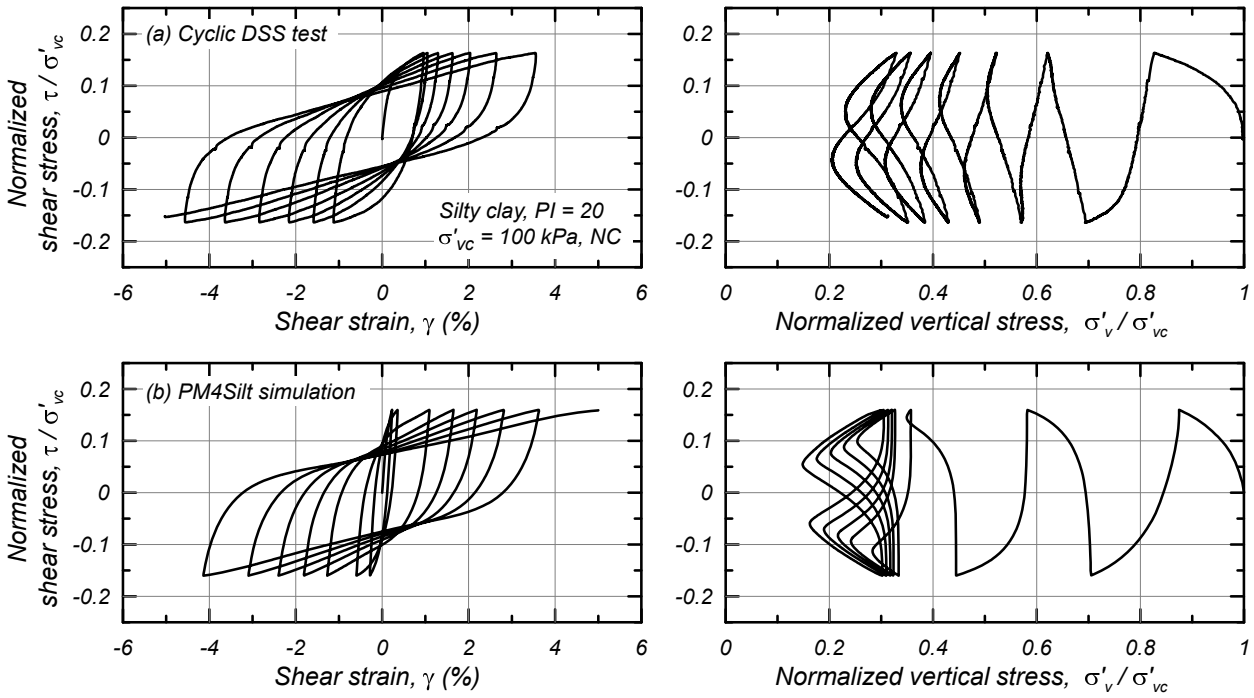

Figure 12. Stress-strain and stress path responses in cyclic undrained stress-controlled DSS loading for a slurry sedimented, normally consolidated silty clay with PI = 20 (Boulanger et al. 2018).

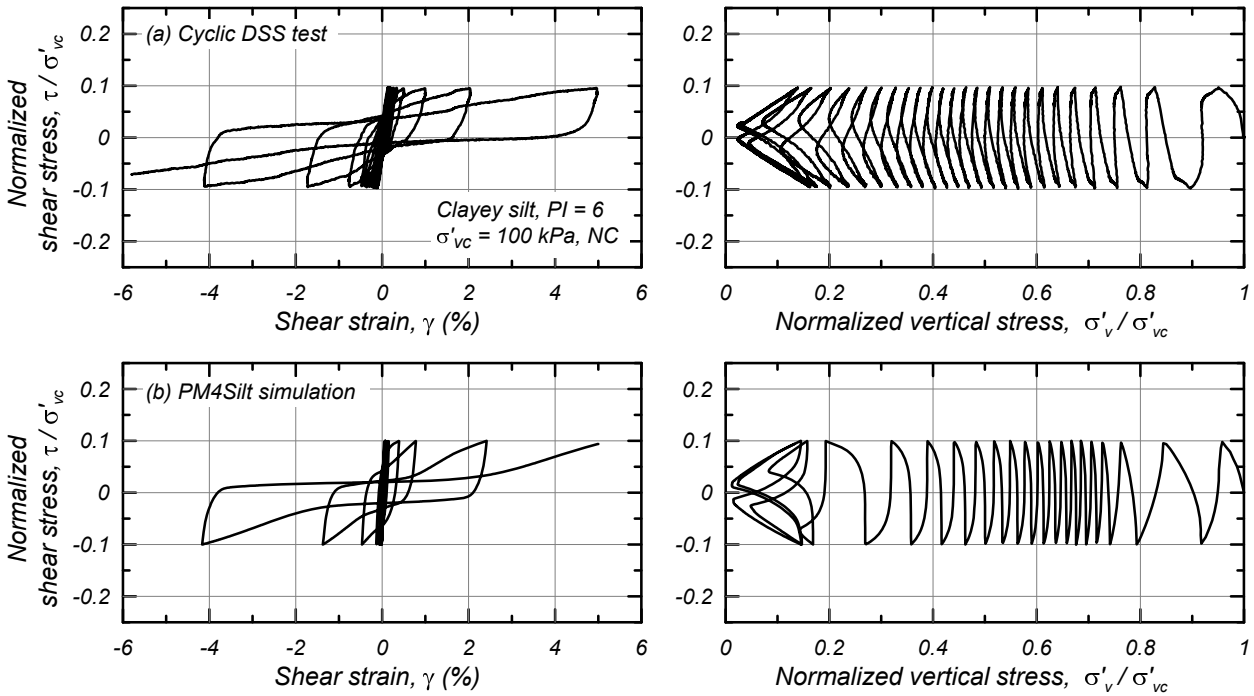

Figure 13. Stress-strain and stress path responses in cyclic undrained stress-controlled DSS loading for a slurry sedimented, normally consolidated clayey silt with PI = 6 (Boulanger et al. 2018).

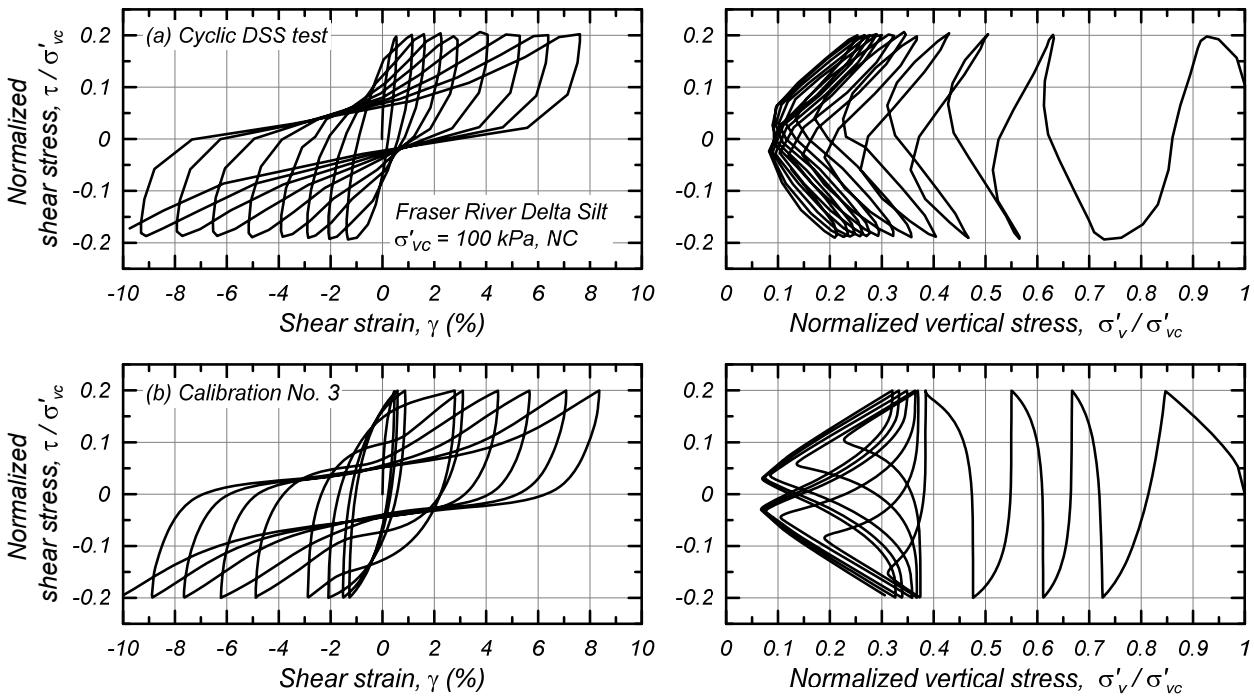

Figure 14. Stress-strain and stress path responses in cyclic undrained stress-controlled DSS loading for field samples of Fraser River Delta Silt with PI = 4 that were normally consolidated in the laboratory (Boulanger and Wijewickreme 2019).

APPENDIX A

Table A1. Constitutive equations for PM4Sand (version 3.1) and PM4Silt

PM4Sand (version 3.1)	PM4Silt model ("- same -" indicates same as for PM4Sand)
Critical state line	***Critical state line***
$\xi_R = \dfrac{R}{Q - \ln\left(100\dfrac{p}{p_A}\right)} - D_R$	$\xi = e - \Gamma + \lambda \ln\left(\dfrac{p}{F_{su}\cdot 1kPa}\right)$ $F_{su} = 1.0$ *at initialization*
Elastic deviatoric strain increment	***Elastic deviatoric strain increment***
$d\boldsymbol{e}^{el} = \dfrac{d\boldsymbol{s}}{2G}$	- same -
$G = G_o p_A \left(\dfrac{p}{p_A}\right)^{1/2} C_{SR}\left(\dfrac{1+\dfrac{z_{cum}}{z_{max}}}{1+\dfrac{z_{cum}}{z_{max}}C_{GD}}\right)$	$G = G_o p_A \left(\dfrac{p}{p_A}\right)^{n_G} C_{SR}\left(\dfrac{1+\dfrac{z_{cum}}{z_{max}}}{1+\dfrac{z_{cum}}{z_{max}}C_{GD}}\right)$
$C_{SR} = 1 - C_{SR,o}\cdot\left(\dfrac{M}{M^b}\right)^{m_{SR}}$	- same -
$C_{SR,o} = 0.5$	- same -
$m_{SR} = 4$	- same -
Elastic volumetric strain increment	***Elastic volumetric strain increment***
$d\varepsilon_v^{el} = \dfrac{dp}{K}$	- same -
$K = \dfrac{2(1+v)}{3(1-2v)}G$	- same -
Yield surface	***Yield surface***
$f = \left[(\boldsymbol{s} - p\boldsymbol{\alpha}):(\boldsymbol{s} - p\boldsymbol{\alpha})\right]^{1/2} - \sqrt{1/2}\,pm = 0$	- same -
$m = 0.01$	- same -
Plastic deviatoric strain increment	***Plastic deviatoric strain increment***
$d\boldsymbol{e}^{pl} = \langle L\rangle \boldsymbol{R}'$	- same -
$\boldsymbol{R} = \boldsymbol{R}' + \dfrac{1}{3}D\boldsymbol{I} = \boldsymbol{n} + \dfrac{1}{3}D\boldsymbol{I}$	- same -
$M = 2\cdot\sin(\phi_{cv})$	- same -
$M^b = M\cdot\exp\left(-n^b\xi_R\right)$	$M^b = M\cdot\exp\left(-n^{b,wet}\dfrac{\xi}{\lambda}\right) \quad for \quad \xi \geq 0$ $= M\cdot\left(\dfrac{1+C_{Mb}}{\dfrac{p}{p_{cs}}+C_{Mb}}\right)^{n^{b,dry}} \quad for \quad \xi < 0$ $C_{Mb} = \dfrac{1}{\left(\dfrac{M^{b,\max}}{M}\right)^{1/n^{b,dry}} - 1}$ $M^{b,\max} = 2\cdot\sin(\phi_{\max})$

	$\phi_{\max} = 60°$
$\boldsymbol{\alpha}^b = \sqrt{1/2}\left[M^b - m\right]\boldsymbol{n}$	- same -
$K_p = G \cdot h_o \dfrac{\left[\left(\boldsymbol{\alpha}^b - \boldsymbol{a}\right):\boldsymbol{n}\right]^{0.5}}{\left[\exp\left(\left(\boldsymbol{\alpha} - \boldsymbol{a}_{in}\right):\boldsymbol{n}\right) - 1\right] + C_{\gamma 1}} C_{rev} \cdot \dfrac{C_{k\alpha}}{1 + C_{K_p}\left(\dfrac{z_{peak}}{z_{\max}}\right)\left\langle\left(\boldsymbol{\alpha}^b - \boldsymbol{a}\right):\boldsymbol{n}\right\rangle\sqrt{1 - C_{zpk2}}}$	- same -
$C_{rev} = \dfrac{\left(\boldsymbol{\alpha} - \boldsymbol{\alpha}_{in}^{app}\right):\boldsymbol{n}}{\left(\boldsymbol{\alpha} - \boldsymbol{\alpha}_{in}^{true}\right):\boldsymbol{n}} \quad for \quad \left(\boldsymbol{\alpha} - \boldsymbol{\alpha}_{in}^{p}\right):\boldsymbol{n} \le \boldsymbol{0}$ $= 1 \quad otherwise$	- same -
$C_{K\alpha} = 1 + \dfrac{C_{K\alpha f}}{1 + \left(2.5 \cdot \left\langle\left(\boldsymbol{\alpha} - \boldsymbol{a}_{in}^{true}\right):\boldsymbol{n}\right\rangle\right)^2} \cdot C_{pzp2} \cdot C_{zpk1}$	- same -
$C_{zpk1} = \dfrac{z_{peak}}{z_{cum} + \dfrac{z_{max}}{5}}$	- same -
$C_{zpk2} = \dfrac{z_{peak}}{z_{cum} + \dfrac{z_{max}}{100}}$	- same -
$C_{pzp2} = \dfrac{-\left\langle-\left(p_{zp} - p\right)\right\rangle}{-\left\langle-\left(p_{zp} - p\right)\right\rangle + p_{\min}}$	- same -
$C_{\gamma 1} = \dfrac{h_o}{200}$	- same -
$C_{Kp} = 2$	- same -
Plastic volumetric strain increment	***Plastic volumetric strain increment***
$d\varepsilon_v^{pl} = \left\langle L\right\rangle D$	- same -
$M^d = M \cdot \exp\left(n^d \xi_R\right)$	$M^d = M \cdot \exp\left(n^d \dfrac{\xi}{\lambda}\right)$
$M^{dR} = \dfrac{M^d}{C_{rot1}}$	- same -
$C_{rot1} = 1 + \dfrac{2 \cdot \left\langle-\boldsymbol{z}:\boldsymbol{n}\right\rangle}{\sqrt{2} z_{\max}} \cdot \left(1 - C_{zin1}\right) \ge 1$	- same -
$C_{zin1} = \left\langle 1 - \exp\left(-2.0\left\lvert\dfrac{\boldsymbol{z}_{in}:\boldsymbol{n} - \boldsymbol{z}:\boldsymbol{n}}{z_{\max}}\right\rvert\right)\right\rangle$	- same -
$\alpha^d = \dfrac{1}{\sqrt{2}} \cdot \left(M^d - m\right)\boldsymbol{n}$	- same -
$\alpha^{dR} = \dfrac{1}{\sqrt{2}} \cdot \left(M^{dR} - m\right)\boldsymbol{n}$	- same -
If dilating (D<0):	***If dilating (D<0):***
$D_{non-rot} = A_d \cdot \left[\left(\boldsymbol{\alpha}^d - \boldsymbol{\alpha}\right):\boldsymbol{n}\right]$	- same -

$D_{rot} = A_d \cdot \frac{\langle -\boldsymbol{z} : \boldsymbol{n} \rangle}{\sqrt{2} z_{\max}} \cdot \frac{(\alpha^{dR} - \alpha) : \boldsymbol{n}}{C_{DR}}$	- same -
$if \;\; D_{non-rot} < D_{rot} \;\; \Rightarrow \;\; D = D_{non-rot}$	
$else \;\; D = D_{non-rot} + \left(D_{rot} - D_{non-rot} \right) \cdot \frac{\left\langle M^b - M^{cur} \right\rangle}{\left\langle M^b - M^{cur} + 0.01 \right\rangle}$	- same -
$A_d = \frac{A_{do}\left(C_{zin2}\right)}{\left(\frac{z_{cum}^2}{z_{\max}}\right)\left(1 - \frac{\langle -\boldsymbol{z} : \boldsymbol{n} \rangle}{\sqrt{2} \cdot z_{peak}}\right)^3 \left(C_{\varepsilon}\right)^2 \left(C_{pzp}\right)\left(C_{p\min}\right)\left(C_{zin1}\right) + 1}$	- same -
$A_{do} = \frac{1}{0.4} \cdot \frac{\left[\sin^{-1}\left(\frac{M^b}{2}\right) - \sin^{-1}\left(\frac{M}{2}\right) \right]}{M^b - M^d}$	- same -
$C_{pzp} = \frac{1}{1 + \left(2.5 p \,/\, p_{zp} \right)^5}$	- same -
$C_{p\min} = \frac{1}{1 + \left(p_{\min} \,/\, p \right)^2}$	- same -
$C_{zin1} = \left\langle 1 - \exp\left(-2.0 \left| \frac{\boldsymbol{z}_{in} : \boldsymbol{n} - \boldsymbol{z} : \boldsymbol{n}}{z_{max}} \right| \right) \right\rangle$	- same -
$C_{zin2} = \frac{1 + C_{zin1} \frac{z_{cum} - z_{peak}}{3 z_{max}}}{1 + 3 C_{zin1} \frac{z_{cum} - z_{peak}}{3 z_{max}}}$	- same -
If contracting (D≥ 0)	***If contracting (D≥ 0)***
$D = A_{dc} \cdot \left[\left(\boldsymbol{\alpha} - \boldsymbol{\alpha}_{in}^{app} \right) : \boldsymbol{n} + C_{in} \right]^2 \frac{\left(\boldsymbol{\alpha}^d - \boldsymbol{\alpha} \right) : \boldsymbol{n}}{\left(\boldsymbol{\alpha}^d - \boldsymbol{\alpha} \right) : \boldsymbol{n} + C_D} C_{p\min 2}$	$D = A_{dc} \cdot \left[\left(\boldsymbol{\alpha} - \boldsymbol{\alpha}_{in}^{app} \right) : \boldsymbol{n} + C_{in} \right]^2 \frac{\left(\boldsymbol{\alpha}^d - \boldsymbol{\alpha} \right) : \boldsymbol{n}}{\left(\boldsymbol{\alpha}^d - \boldsymbol{\alpha} \right) : \boldsymbol{n} + C_D} C_{p\min}$
$\leq 1.5 \cdot A_{do} \frac{\left(\boldsymbol{\alpha}^d - \boldsymbol{\alpha} \right) : \boldsymbol{n}}{\left(\boldsymbol{\alpha}^d - \boldsymbol{\alpha} \right) : \boldsymbol{n} + C_D}$	$\leq A_{do} \frac{\left(\boldsymbol{\alpha}^d - \boldsymbol{\alpha} \right) : \boldsymbol{n}}{\left(\boldsymbol{\alpha}^d - \boldsymbol{\alpha} \right) : \boldsymbol{n} + C_D} C_{p\min}$
$A_{dc} = \frac{A_{do}\left(1 + \langle \boldsymbol{z} : \boldsymbol{n} \rangle\right)}{h_p C_{dz}}$	$A_{dc} = \frac{A_{do}\left(1 + \langle \boldsymbol{z} : \boldsymbol{n} \rangle\right)}{h_p C_{dz} C_{wet}}$
$C_{in} = \frac{2 \langle \boldsymbol{z} : \boldsymbol{n} \rangle}{\sqrt{2} z_{max}}$	- same -
$C_{dz} = \left(1 - C_{rot2} \cdot \frac{\sqrt{2} z_{peak}}{z_{max}} \right) \cdot \left(\frac{z_{max}}{z_{max} + C_{rot2} z_{cum}} \right) \geq \frac{1}{1 + \frac{z_{max}}{2}}$	- same -
$C_{rot2} = 1 - \frac{z_{peak}}{z_{cum} + \frac{z_{max}}{100}} \left(= 1 - C_{zpk2} \right)$	- same -
$C_D = 0.1$	- same -

	$C_{wet} = \dfrac{1}{\dfrac{1}{1+\left(\dfrac{C_{w1}}{(\alpha^b-\alpha):\mathrm{n}}\right)^4}+\dfrac{1}{1+\left(\dfrac{\xi/\lambda}{C_{w2}}\right)^2}} \le 1$ $C_{w1} = 0.02$ $C_{w2} = 0.1$
$C_{p\min 2} = 0 \quad for \quad p \le 2p_{\min}$ $= 1 \quad for \quad p \ge 18p_{\min}$ $= \dfrac{p-2p_{\min}}{16p_{\min}} \quad otherwise$	$C_{p\min} = 0 \quad for \quad p < 2p_{\min}$ $= 1 \quad for \quad p > 8p_{\min}$ $= \dfrac{p-2p_{\min}}{6p_{\min}} \quad otherwise$
$h_p = h_{po}\, exp\left(-0.7+7.0\left(0.5-\xi_R\right)^2\right) \quad for \quad \xi_R \le 0.5$ $h_p = h_{po}\, exp\left(-0.7\right) \quad for \quad \xi_R > 0.5$	$h_p = h_{po} \cdot \exp\left(-0.7+0.2\left(3-\dfrac{\xi}{\lambda}\right)^2\right) \quad for \quad \dfrac{\xi}{\lambda} \le 3$ $h_p = h_{po} \cdot \exp\left(-0.7\right) \quad for \quad \dfrac{\xi}{\lambda} > 3$
	If $p < 2\, p_{min}$ $D = -3.5A_{do}\left\langle M^b - M^d \right\rangle \dfrac{2p_{\min}-p}{p_{\min}}$
Fabric-dilatancy tensor update if $\left(\boldsymbol{\alpha}^d-\boldsymbol{\alpha}\right):\boldsymbol{n}<0$	***Fabric-dilatancy tensor update if*** $\left(\boldsymbol{\alpha}^d-\boldsymbol{\alpha}\right):\boldsymbol{n}<0$
$d\boldsymbol{z} = -\dfrac{c_z}{1+\left\langle \dfrac{z_{cum}}{2z_{max}}-1\right\rangle}\dfrac{\left\langle -d\varepsilon_v^{pl}\right\rangle}{D}\left(z_{max}\boldsymbol{n}+\boldsymbol{z}\right)$	- same -
$dz_{cum} = \lvert d\boldsymbol{z}\rvert$	- same -
Stress increment	***Stress increment***
$L = \dfrac{2G\boldsymbol{n}:d\boldsymbol{e}-\boldsymbol{n}:\boldsymbol{r}Kd\varepsilon_v}{K_p+2G-KD\boldsymbol{n}:\boldsymbol{r}}$	- same -
$d\boldsymbol{\sigma} = 2Gd\boldsymbol{e}+Kd\varepsilon_v\boldsymbol{I}-\langle L\rangle\left(2G\boldsymbol{n}+KD\boldsymbol{I}\right)$	- same -